

ABSTRACT

LANE, BRANDON MICHAEL. Development of Predictive Models for Abrasive and Chemical Wear of Diamond Tools. (Under the direction of Thomas A. Dow).

Diamond machining (DM) was introduced in the early 70s as a means to machine optical quality surfaces without the need for grinding, polishing, or metal coating. Despite its hardness, machining with diamond will ultimately introduce tool wear. This wear has been attributed to abrasive and/or thermo-chemical interactions. Though there is much observational data regarding diamond tool wear, little is known regarding the actual physical mechanisms that cause this wear. This research looks into diamond tool wearing processes and develops techniques to predict tool wear. Methods were studied and developed that enable sub-micrometer measurement of tool wear. Baseline machining experiments were conducted on Al6061 and St1215 including measurement of tool forces and wear. A model for abrasive wear was derived from the Al6061 data that relates measurable tool forces to the degree of tool wear. Wear rates when machining St1215 were considerably higher than that for Al6061 as expected. A unique and previously unreported wear pattern for the 1215 steel was observed. A simple experiment showed that this pattern was related to the cutting direction, and not the crystal orientation. Finite element software was utilized to predict tool temperatures as a function of machining speed and a model was derived that predicts wear rates as a function of these temperatures for St1215. These models provide insight into the diamond tool wearing processes and give direction for modeling wear of other diamond machined materials. Continued wear modeling for other materials may lead to better decisions in diamond tool manufacture and selection of workpiece materials.

Development of Predictive Models for Abrasive
and Chemical Wear of Diamond Tools

by
Brandon Michael Lane

A thesis submitted to the Graduate Faculty of
North Carolina State University
in partial fulfillment of the
requirements for the Degree of
Master of Science

Mechanical and Aerospace Engineering

Raleigh, North Carolina

2010

APPROVED BY:

Ronald Scattergood

Jeff Eischen

Thomas A. Dow
Chair of Advisory Committee

BIOGRAPHY

Brandon Lane was born in Reno, Nevada, in 1984 and grew up in a small town in central Nevada called Battle Mountain, accurately dubbed by the Washington Post as “The Armpit of America”. He graduated as valedictorian (along with his twin sister) from Battle Mountain High School, then pursued a degree in Computer Science at University of Nevada, Reno. A distaste for program debugging and an engineering scholarship led him to more active learning at the Mechanical Engineering department at UNR. He spent his summers working for the Bureau of Land Management as a ground traffic controller for wildland firefighting airtankers, or as a grunt on a wildland fire engine.

Increased focus on engineering led him to an internship with the R&D department Hamilton Company, which designs and manufactures automated fluid-handling devices for medical and biological research purposes. He also was elected as the Vice President of the UNR chapter of Society of Women Engineers after succumbing to persuasion from his female engineering friends. With SWE, he helped organize a regional conference held in Reno. He was also awarded an undergraduate research grant at UNR, and helped develop carbon-based nano-composite manufacturing techniques with Dr. Jonghwan Suhr at the Multifunctional Nano-Composite Lab.

Research experience, a deteriorating job market, and an opportunity to finally leave Nevada led him to pursue graduate school. The Mechanical and Aeronautical Engineering department provided a compelling tour of NC State, and an offer from the Precision Engineering Center finalized his decision to move to Raleigh.

He currently enjoys volunteering at the SPCA, exploring the outdoors in the great NC weather, and teaching Southerners how to correctly pronounce Nevada. He plans to continue research at the PEC and complete his PhD.

ACKNOWLEDGEMENTS

Special thanks to my family for putting up with a son/brother that is thousands of miles away, and is often too busy to remember to call.

Special thanks to Dr. Dow for providing the opportunity, facilities, and mentorship required for a successful graduate career. He provided invaluable lessons on better communication and its requirement for success.

Thanks to Alex Sohn for always being available for instruction on equipment use and letting me know when my presentations are getting boring. Thanks to Ken Garrard for constructing the bulk of the Digitize09 software, and vastly expanding my knowledge of Matlab. Special thanks to Dr. Scattergood and Dr. Eischen for not only being on my committee, but igniting my interest in mechanics of materials, which I had previously dreaded.

Chuck Mooney of the Analytical Instrumentation Facility at NC State provided much knowledge and training, and Meirong Shi of the PEC provided all EBID striping and use of the SEM.

This project was funded by the National Science Foundation contract #CMMI-0800560 monitored by G.Hazelrigg. Diamond tools were supplied by Chardon Tool, and Mike Hunter of Chardon Tool supplied information on industrial diamonds, their manufacturing, and his experiences. Third Wave Systems provided an academic license for the ThirdWave FE software.

TABLE OF CONTENTS

List of Tables	vii
List of Figures	ix
1 Introduction.....	1
1.1 Orthogonal Machining Geometry	3
1.2 Tool Wear Modelling Procedure	5
2 Tool Wear Measurement Techniques	6
2.1 Previous Research	6
2.2 Electron Beam Induced Deposition (EBID) Procedure	8
2.2.1 Image Stretching	10
2.2.2 Stretched Image Measurement with Matlab	13
2.3 Wear Land Measurement with SCANNING White Light Interferometer	15
3 Wear Experiments Machining Al6061	17
3.1 Experimental Setup	17
3.2 Results	21
3.2.1 Depth of Cut Affect on Forces and Chip Formation.....	21
3.2.2 Cutting Forces at 2 μ m DoC	23
3.2.3 Tool Wear Measurements	23
3.3 Discussion.....	27
4 Abrasive Wear Model	28
4.1 Archard Wear and Worn Tool Forces.....	28

4.2	Average Flank Force	30
4.3	Results	31
4.4	Discussion	33
5	Wear Experiments Machining St1215	35
5.1	Experimental Setup	35
5.2	Results	38
5.2.1	Tool Forces	38
5.2.2	EBID Worn Tool Measurements from 2.12 M/s Experiment.....	40
5.2.3	1.06 and 4.24 m/s SWLI wear land measurements	43
5.2.4	Worn Volume Determined from SWLI Wear land Measurements	45
5.3	Conclusions.....	48
6	Crystallographic Affects of Diamond Machining	50
6.1	Crystal Orientation of Diamond Cutting Tools	50
6.2	Crystal Orientation Affects on Wear	53
6.3	Inverted Tool Experiment.....	56
6.3.1	Observed Faces and Nominal Faces	56
6.3.2	Tool Orientation and Cutting Conditions.....	57
6.3.3	Wear Results	59
6.4	Conclusions.....	61
7	Chemical Wear Model	62
7.1	The Arrhenius Equation and Fick's Law	64
7.2	Cutting Tool Temperatures	65

7.3	Finite Element Analysis for Tool Temperatures	67
7.3.1	AdvantEdge Finite Element Modelling	68
7.3.2	St1215 AdvantEdge Cutting Model.....	69
7.3.3	FEM Model Validation	72
7.4	Results	77
7.4.1	AdvantEdge Simulation Results	77
7.5	Discussion.....	79
8	Conclusion	81
9	References	84
10	Appendices.....	87
10.1	Tool Force and Wear data for Experiments on Al6061.....	88
10.2	Tool Force and Wear data for Chemical Wear Experiments on St1215	89
10.3	AdvantEdge FE Cutting Simulation Data	91

LIST OF TABLES

Table 3-1:	Material and cutting properties for abrasive wear experiments	18
Table 5-1:	Material and cutting properties for steel wear experiments.	35
Table 5-2:	Experimental values used to determine EBID wear land to EBID worn area transfer function	46
Table 5-3:	Comparison of measured EBID worn areas to worn areas determined from applying transfer functions to wear lands measured via SWLI.	47
Table 6-1:	Comparison of wear when rubbing $\langle 100 \rangle$ and $\langle 110 \rangle$ directions on a (001) plane from [25]	53
Table 6-2:	Comparison of wear rates for a tilted (001) surface rubbing in the $\langle 100 \rangle$ and $\langle 110 \rangle$ directions from [26].	54
Table 6-3:	Comparison of rake and flank nomenclature for standard cutting and the inverted cutting experiment.	57
Table 7-1:	Material and thermal properties of diamond.....	69
Table 7-2:	Comparison of material properties for 1215 Steel (used in experiments) and 1118 steel (available in AdvantEdge material library)	70
Table 10-1:	Force data for multiple depth of cut machining Al6061	88
Table 10-2:	Force data for Al6061, 2 μ m depth of cut	88
Table 10-3:	Wear measurements for Al6061, 2 μ m depth of cut	88
Table 10-4:	Determination of Archard Wear coefficient for diamond tool machining Al6061	88
Table 10-5:	Force data for St1215, 1 μ m depth of cut, 2 m/s machine speed.....	89

Table 10-6:	Wear measurements for St1215, 1 μm depth of cut, 2 m/s machine speed.	89
Table 10-7:	Force data for St1215, 1 μm depth of cut, 1 and 4 m/s machine speed	89
Table 10-8:	SWLI Wear land to EBID Worn Area conversion calculations,.....	90
Table 10-9:	AdvantEdge FE cutting model verification. Tool forces for St1118 at 1 μm depth of cut, 2.12 m/s machine speed	91
Table 10-10:	AdvantEdge FE cutting model verification. Determination of friction angle for St1118 at 1 μm depth of cut, 2.12 m/s machine speed	91
Table 10-11:	AdvantEdge FE cutting model verification. Shear angle, max tool temp, and shear angle for St1118 at 1 μm depth of cut, 2 m/s machine speed.	91
Table 10-12:	AdvantEdge FE cutting model maximum tool temperature for St1118, 1 μm depth of cut.....	92

LIST OF FIGURES

Figure 1-1:	Schematic of orthogonal cutting geometry with the tool edge narrower than the workpiece.	3
Figure 1-2:	Schematic showing worn tool nomenclature. Tool shown has 0 degree rake angle.....	4
Figure 2-1:	Example SEM image of worn diamond tool with and without EBID stripe.	7
Figure 2-2:	Platinum ion stripes used to distinguish sharp diamond edge. Resolution of the stripe edge was inferior to EBID stripes.	7
Figure 2-3:	SEM sample holder constructed for diamond tools used in cutting experiments.	8
Figure 2-4:	Angular dimensions of SEM sample holder. Dotted lines show contacts that restrict pitch and roll (left) and rotation around the fastener (right).	9
Figure 2-5:	EBID stripe is made by scanning across the tool edge with a 45° tilt about X.	9
Figure 2-6:	Tilting the sample 45° about Z allows tool edge pseudo-cross section to be viewed.....	10
Figure 2-7:	An image object will have a height L when viewed straight on or from the side	11
Figure 2-8:	Image of a tilted object will have height L' (left). Skewing the image vertically will retain the true measurable height of the object, L	11
Figure 2-9:	Example of SEM-EBID image being stretched vertically. EBID stripe in right image correctly traces the tool edge cross section	12
Figure 2-10:	Process to recreate worn tool cross-section from EBID images.....	13

Figure 2-11:	Digitize09 allows a user to select individual pixels (blue dots) along the EBID stripe. These pixels are used to calculate wear land, edge radius, and scaling (<i>left</i>) and worn area and included tool angle (<i>right</i>).	14
Figure 2-12:	Diamond tool is tilted to allow the wear land to be measured by a SWLI (<i>left</i>). Zygo NewView monitor showing fringes along the wear land (<i>upper right</i>). 15	15
Figure 2-13:	Metropro image showing a wear land being measured. Calipers on the lower image measure the top-most slice of the upper image.	16
Figure 3-1:	Holder dimensions for replaceable Al6061 disks (<i>left</i>) and setup for orthogonal cutting (<i>right</i>).	18
Figure 3-2:	Diamond tool post incorporating a 3-axis piezoelectric load cell for dynamic force measurement [5].	19
Figure 3-3:	ASG-2500 diamond turning machine and control center.....	20
Figure 3-4:	Example force measurement taken during plunge (<i>top</i>) and backout (<i>bottom</i>) during cutting Al6061 at 2.5 μ m depth of cut.	21
Figure 3-5:	Initial cutting experiments at varying depth of cut with a sharp tool on Al6061.	22
Figure 3-6:	Clustered chips on the diamond tool while cutting Al6061 at 2.5 μ m DoC. ..	22
Figure 3-7:	Tool forces measured while cutting Al6061. Error bars show one standard deviation.	23
Figure 3-8:	EBID image of sharp tool (<i>top</i>) and worn after cutting 2.5 km (<i>lower left</i>) and 10 km (<i>lower right</i>) of Al6061.	24
Figure 3-9:	Traced EBID stripes of diamond tool after cut distances of 2.5, 5, 7.5 and 10 km cut distance on Al6061.....	25
Figure 3-10:	Wear geometry measured from EBID images after cutting Al6061.	25

Figure 3-11:	Wear volume of diamond tool cutting Al6061.	26
Figure 4-1:	Schematic of worn diamond tool, average forces acting on the tool, and resultant tool forces.....	29
Figure 4-2:	Archard wear constant determined for diamond machining of Al6061	32
Figure 5-1:	St1215 workpiece used in orthogonal turning experiments.....	36
Figure 5-2:	Cutting and thrust forces measured during 2.12 m/s cut experiments on St1215. Error bars show one standard deviation.	38
Figure 5-3:	Cutting force signal as tool chattering developed. Chattering started at approximately 80 m of cutting at 1.06 m/s.	39
Figure 5-4:	Measured tool forces for 1.06 and 4.24 m/s machining speeds on St1215. Error bars show one standard deviation.	39
Figure 5-5:	EBID image of sharp tool (top) and tool worn after cutting 5m (lower left) and 20m (lower right) of St1215 steel at 2.12 m/s.....	40
Figure 5-6:	Edge radius and wear land measurements made from EBID images of tool worn after cutting St1215.....	41
Figure 5-7:	Worn volume determined from Digitize09 EBID image analysis of tool worn after cutting St1215 at 2.12 m/s.....	41
Figure 5-8:	Traced EBID stripes of diamond tool after cut distances of 5, 10, 15 and 20 m cut distance on St1215.....	42
Figure 5-9:	Traced EBID stripes of St1215 and Al6061 worn tools. Tool wear profile for St1215 worn tool exhibits an upturned wear land compared to Al6061-worn tool.....	43
Figure 5-10:	Measured wear land length vs. cut distance after cutting St1215 at two cutting velocities.	44

Figure 5-11:	Measured wear land length vs. machining time after cutting St 1215 at two cutting velocities. The last three data points of the 1.06 m/s are removed due to tool chattering.	45
Figure 5-12:	Transfer function determined that converts SWLI wear land measurements to equivalent EBID wear land measurements.	46
Figure 5-13:	Transfer function determined that converts EBID wear land measurements to equivalent EBID worn area for diamond tools worn by St1215 in this study	47
Figure 5-14:	Wear land measurements converted to equivalent EBID worn volume vs. cut time.	48
Figure 6-1:	Model of a cubic element of the diamond lattice.	50
Figure 6-2:	Cubic diamond planes are geometrically equivalent and can all be noted as (001) planes.....	51
Figure 6-3:	Directional symmetries on the (001) family of planes in the diamond crystal lattice: <100> directions (left) and <110> directions.....	51
Figure 6-4:	A (001) plane lapped to form a flank face of a cutting tool.....	52
Figure 6-5:	Reoriented crystal from Figure 6-4 showing relationship to cutting tool geometry.....	52
Figure 6-6:	Schematic describing rubbing directions with respect to surfaces tilted about the true crystal planes.	54
Figure 6-7:	Schematic of tool orientation in standard cutting.....	56
Figure 6-8:	Schematic of tool orientation during inverted cutting.	57
Figure 6-9:	Straightedge protractor (A) used to roughly align the tool rake face (B) by 84° from the DTM stage (C)	58

Figure 6-10:	Stretched EBID image of tool used in standard cutting St1215 (left) and inverted cutting (right) at 2.12 m/s and 1 μm DoC for 5m cut distance	59
Figure 6-11:	Worn tool cross sections traced from EBID images with crystal orientations aligned.....	60
Figure 6-12:	Worn tool cross sections traced from EBID images with cut directions aligned	61
Figure 7-1:	Schematic of heat transfer model in orthogonal cutting considering combined effects of three heat sources from Abukhshim et. al. [28].....	66
Figure 7-2:	Mesh and boundary conditions for the AdvantEdge cutting model	71
Figure 7-3:	(Left) Stretched EBID image of diamond tool worn after 10 m distance at 2 m/s and 1 μm depth of cut. (Right) Tool dimensions are replicated in FEM model.	71
Figure 7-4:	Affects of varying friction coefficient in AdvantEdge FE 1118 steel model. Error bars show one standard deviation.	72
Figure 7-5:	Change in ratio of cutting force to thrust force with friction coefficient for 4 AdvantEdge cutting simulations of St1118.....	73
Figure 7-6:	Chip sizes for 4 values of friction coefficient in AdvantEdge St1118 simulation.	73
Figure 7-7:	SEM image of chip edge collected after machining St1215 at 2 m/s and 1 μm depth of cut.....	74
Figure 7-8:	AdvantEdge simulated chip width compared to those measured experimentally.	74
Figure 7-9:	Maximum tool temperature determined from AdvantEdge simulations cutting St1118 for varying friction coefficient. Standard deviation of data noise is < 0.25°C.....	75

Figure 7-10: AdvantEdge simulation as a function of cutting speed for 1118 steel at 1 μ m DoC..... 76

Figure 7-11: Steady state temperature contour plot of 1.06 m/s (left) and 4.24 m/s (right) simulations..... 77

Figure 7-12: Predicted cutting forces and maximum tool temperatures for 1.06 m/s (left) and 4.24 m/s (right) 78

Figure 7-13: Arrhenius plot of diamond tool wear on low carbon steel 79

1 INTRODUCTION

Diamond machining (DM) was introduced in the early 70s as a means for producing optical quality surface finishes without the need for grinding or polishing. Diamond has characteristics that make it perfect for this purpose. Diamond is extremely hard, making it resistant to abrasive wear and can be lapped to very sharp, very smooth cutting edge. When used to cut another material, these smooth cutting edges are reproduced in the material, which produces the optical surface finish. Diamond tools are also used in the ruling of diffraction gratings, or manufacture of microscopic features which require high geometric accuracy.

Like all contacting and rubbing materials, diamond will wear. This increase in wear causes degradation in surface finish on the machined part. As the tool wears, the reproduced cutting edge determines the change in surface geometry.

There is little research regarding the wear of diamond on materials commonly used in diamond turning. Crompton, Hirst, and Howse [1] gave one of the first studies on the rubbing of diamond on various materials, and showed that the wear follows a well-known law derived by Archard [2]. Their experiments involved relatively flat surfaces, and do not directly predict that the wear of diamond tools will follow Archard's wear law. Wilks and Wilks [3] compiled the most extensive review of diamond and its use in industrial processes. They also failed to note any direct relationship between measured tool wear and Archard's wear law.

Drescher [4] developed a technique that enabled the microscopic wear pattern of diamond tools to be accurately measured and used measured tool forces as well as wear patterns to develop an empirical tool force model [5]. He used this model to calculate the tool wear and the expected surface finish from measured tool forces. Arcona [6] built upon Drescher's tool force model by incorporating a method for observing shear angles in the chip formation process and an empirical model for elastic recovery behind the tool.

Drescher's and Arcona's models predicted wear and tool forces respectively within 50% for new or only slightly worn tools. Both models, however, lost accuracy with further amounts of wear. They only enveloped the diamond turning process, and neglected more standardized wear models such as Archard's. Drescher's and Arcona's models didn't address the mechanisms causing wear, only affects on tool forces and surface finish. Their results cannot be directly compared with wear results from non-diamond machining experiments, nor address the physical wearing mechanisms that occur in the cutting process.

Extensive research has been done regarding the wear of diamond on ferrous alloys such as steel. Steel in its various forms is a widely used engineering material, but causes extremely high rates of wear to diamond. Consensus was made early in diamond turning history [6,8] that the high rate of wear was due to the chemical surface interactions of diamond and ferrous materials.

Relating wear to the chemical properties of workpiece material wasn't accomplished until Paul and Evans, et. al. [9] noticed a correlation between wear rates and the number of unpaired d-shell electrons in the constituent elements of workpiece materials. The loss of diamond volume due to chemical processes is commonly assumed to occur from diffusion of carbon from the diamond into the workpiece, graphitization of the diamond (change of solid state to a lower energy phase) catalyzed by the workpiece material, or a combination of both. Paul and Evans noted that diffusion, following Fick's law, and graphitization, following the Arrhenius Law, can both be described by the same equation. The equation depends on temperature, however, which is not easily modeled in the machining process. Since direct measurement of workpiece and tool temperatures or accurate modeling is difficult, direct correlation of diamond tool wear and tool temperatures through the Arrhenius equation has not been accomplished.

1.1 ORTHOGONAL MACHINING GEOMETRY

Diamond machining can be done with the tool situated at various geometries with respect to the workpiece. The relative orientations of the tool and workpiece affect nearly every aspect of the machining process including chip formation, tool forces, and surface finish and can be tailored to produce desired results. The cutting process is simplified when orthogonal cutting geometry is used. Figure 1-1 shows a schematic of the orthogonal cutting geometry. In orthogonal cutting, front of the tool and cutting edge are aligned with the toolpath and depth of cut.

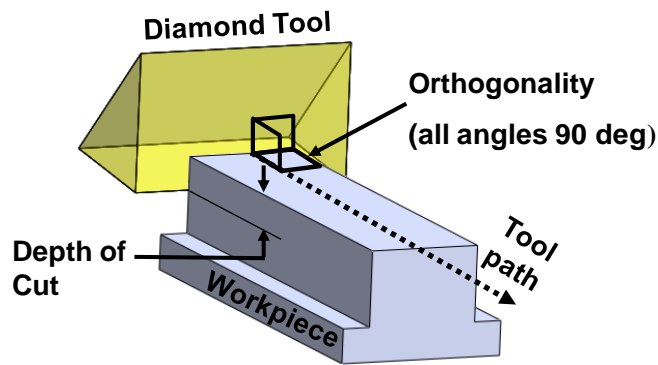


Figure 1-1: Schematic of orthogonal cutting geometry with the tool edge narrower than the workpiece.

Orthogonal cutting allows the cutting process to be modeled as a two-dimensional process. Of course, the process will not be two dimensional near the sides of the workpiece where the tool is no longer cutting. If the workpiece width is much larger ($> 10x$) than the depth of cut, these edge effects can be neglected. If all applied loads on a volume occur in two dimensions and the length of the volume in the third dimension is more than an order of magnitude larger than the lengths in the other two, an assumption of plane strain can be made.

Tool wear is described by certain features. As the tool wears, the sharp cutting edge becomes more round, changing the edge radius¹. Figure 1-2 shows a two-dimensional schematic of the cutting process, with tool geometry and process nomenclature.

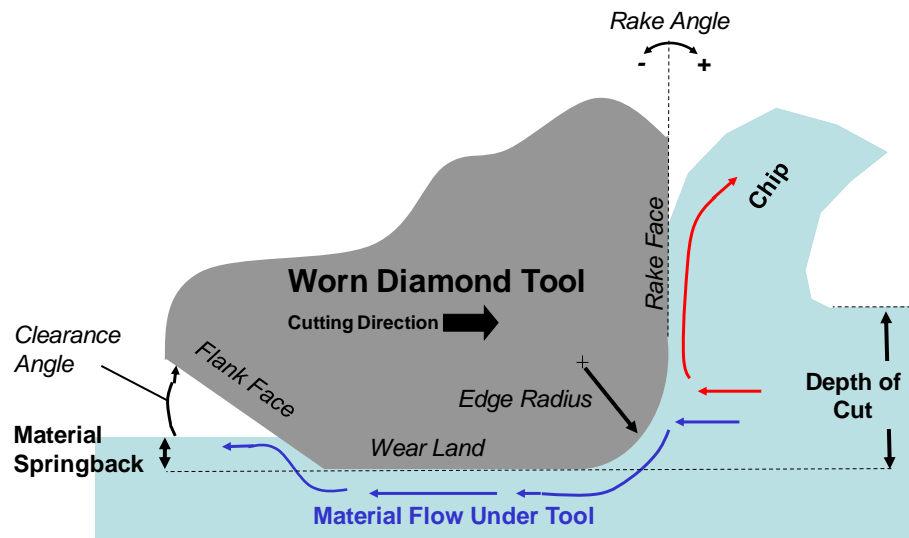


Figure 1-2: Schematic showing worn tool nomenclature. Tool shown has 0 degree rake angle.

If the cutting edge of the tool is not aligned with the top of the workpiece, this will make the depth of cut vary along the width of the tool. By aligning these features, the depth of cut is held constant. If the rake face of the tool is not aligned with the cutting direction, oblique cutting will occur. While oblique cutting has benefits such as reduced forces, it complicates the process by creating lateral workpiece material flow (or chip formation) along the cutting edge. Also, if the rake face of the tool is pitched about the cutting direction, a negative or positive rake angle will occur. Changing the rake angle still allows

¹ Edge radius (of the cutting edge) shouldn't be confused with nose radius, which describes a manufactured round shape of the tool.

the process to be modeled in 2-D, but affects the angle of the shear zone in the chip. This alters the chip thickness, machining forces, and wear of the tool.

1.2 TOOL WEAR MODELLING PROCEDURE

The results given in this thesis are presented as follows:

1. Methods for tool wear characterization are developed, including electron beam induced deposition (EBID) and wear land measurement via scanning white light interferometer (SWLI). Explanations of two techniques and their inherent advantages and limits are given.
2. Cutting experiments are outlined on abrasive and chemical wearing materials. Tool forces and tool wear are measured during successive cuts to show how they are affected by tool wear. These results are used to postulate models for each wear mechanism.
3. Models are created using cutting experiment information and arguments stemming from previous research into abrasive and chemical wearing mechanisms. These models are applied to baseline data, and may be used to predict future diamond wear scenarios.

2 TOOL WEAR MEASUREMENT TECHNIQUES

2.1 PREVIOUS RESEARCH

Previous research has been attempted to accurately measuring the sub-micrometer geometry of worn diamond tools. Asai et. al. [10] developed a technique using two secondary electron detectors in an SEM. This technique was able to precisely trace the cutting edge profile, but required special equipment. Indirect techniques involve measuring tool tip indentations in copper via atomic force microscope (AFM) [11]. Indentation techniques may experience errors from elastic recovery or anisotropy of the indented material. The diamond edge can be also measured directly via AFM [12], though locating the tool edge with the AFM probe requires special alignment equipment. Both techniques using AFM require precise knowledge of the radius of the probe tip.

A method for directly observing and measuring the wear of diamond tools was developed by Drescher [4] in the early 90's. The electron beam induced deposition (EBID) method makes use of hydrocarbon contamination lines that grow on the diamond when a low voltage electron beam is scanned across the tool edge in an SEM chamber. Figure 2-1 gives an example of an EBID image. This the EBID line creates contrast along the tool edge, which in turn can be measured; SEM images without this contrast only allow subjective observation, and the tool edge profile cannot be distinguished.

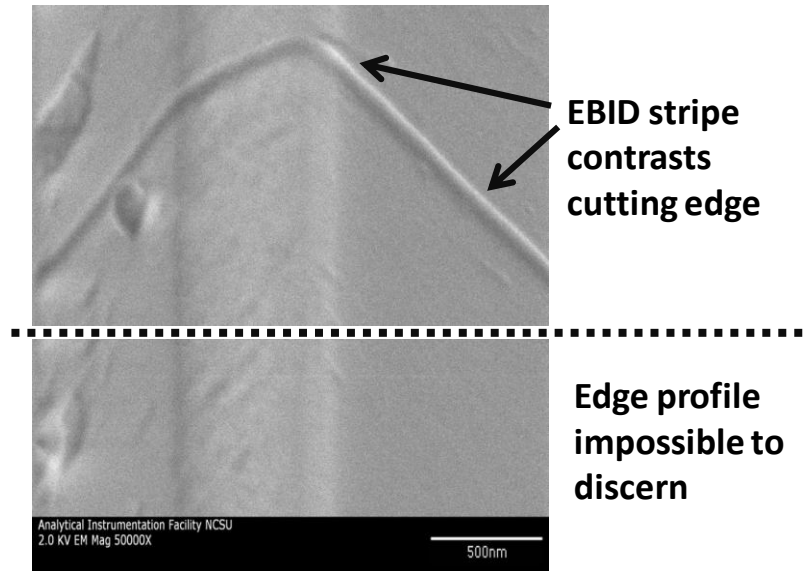


Figure 2-1: Example SEM image of worn diamond tool with and without EBID stripe.

Another method was also attempted that is similar to EBID. A sharp diamond tool was observed in a focused ion beam (FIB) microscope. This system allows sub-micron scale platinum ion deposition onto samples. Platinum deposition stripes were put onto a sharp diamond edge, similar to the EBID process. Figure 2-2 shows the results of the platinum deposition.

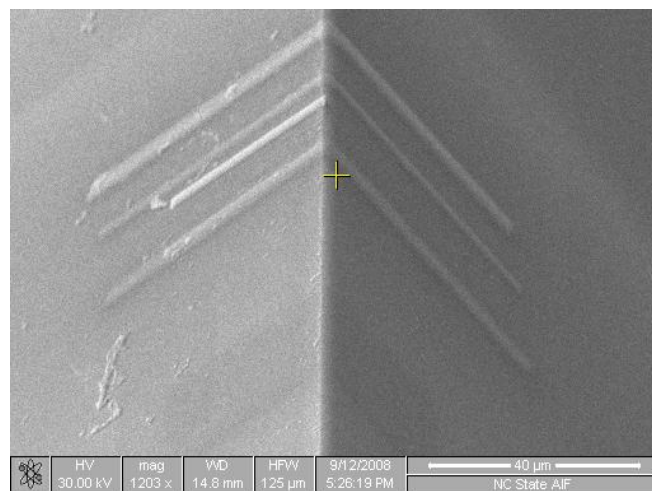


Figure 2-2: Platinum ion stripes used to distinguish sharp diamond edge. Resolution of the stripe edge was inferior to EBID stripes.

The platinum ion deposition is easier to control than EBID. EBID line growth depends on the availability of contaminants in the SEM chamber. However, the resolution of the platinum stripe edge is inferior to that of EBID stripes. The platinum stripe deposition requires tens of minutes and use of the FIB system is expensive. The EBID striping process is the preferred technique and used throughout this study.

2.2 ELECTRON BEAM INDUCED DEPOSITION (EBID) PROCEDURE

During the EBID process, the tool needs to be pitched at a known angle, preferably 45° . An SEM sample stage was machined from Al6061 that includes a M2.5-0.45 tapped hole, shown in Figure 2-3 to hold the diamond tool insert. The diamond tools for this study were mounted on DCMB² (55° diamond shaped) carbide insert.

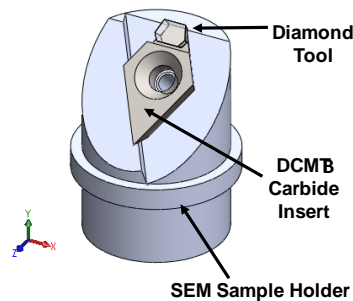


Figure 2-3: SEM sample holder constructed for diamond tools used in cutting experiments.

The EBID process requires that the tool be repeatedly tilted to prescribed angles. The SEM sample holder was designed so that the DCMB insert is kinematically restricted from rotation or translation. Figure 2-4 shows these restrictions and highlights the machined features that cause them. Machined angular dimensions may be inaccurate to a degree or

² The DCMB insert is a standalone carbide machining tool with a diamond brazed on it. DCMB is the ANSI designation for machine tool inserts. D designates the 55° diamond shape, C designates a 7° clearance angle, M designates dimensional tolerance better than $0.005''$, and B designates the countersunk hole and no chip-breaker grooves.

more, depending on the accuracy of the machine and process that made them, but the location of the tool on the SEM sample holder is highly repeatable.

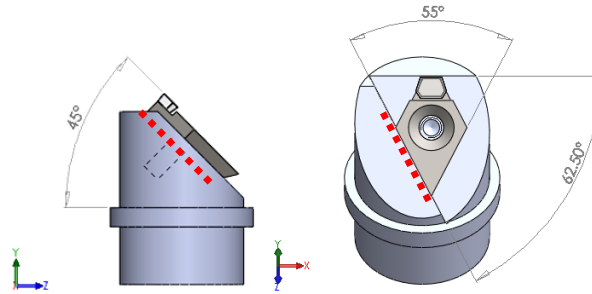


Figure 2-4: Angular dimensions of SEM sample holder. Dotted lines show contacts that restrict pitch and roll (left) and rotation around the fastener (right).

In the SEM chamber, the sample stage is kept horizontal, and a focused electron beam is scanned perpendicular to the tool edge. This causes hydrocarbon contaminants within the SEM chamber to form along the scanned line. Figure 2-5 shows this process. The EBID stripe is placed in a location on the tool edge where wear measurements need to be taken. The amount of time the striping requires depends on the level of contamination within the chamber, and varies with each tool measurement. SEM settings used in this process can be found in [4] and [13].

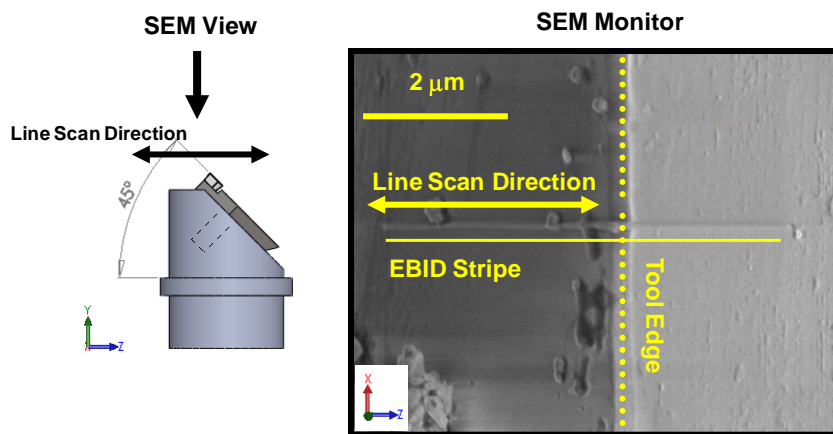


Figure 2-5: EBID stripe is made by scanning across the tool edge with a 45° tilt about X.

After the stripe is made, the SEM sample stage is tilted by 45° . Figure 2-6 shows how this is performed. The zoom of the SEM monitor may need to be reduced while this occurs, therefore it is important that the location of the EBID stripe along the tool edge be noted so that it can be found again after the tilt.

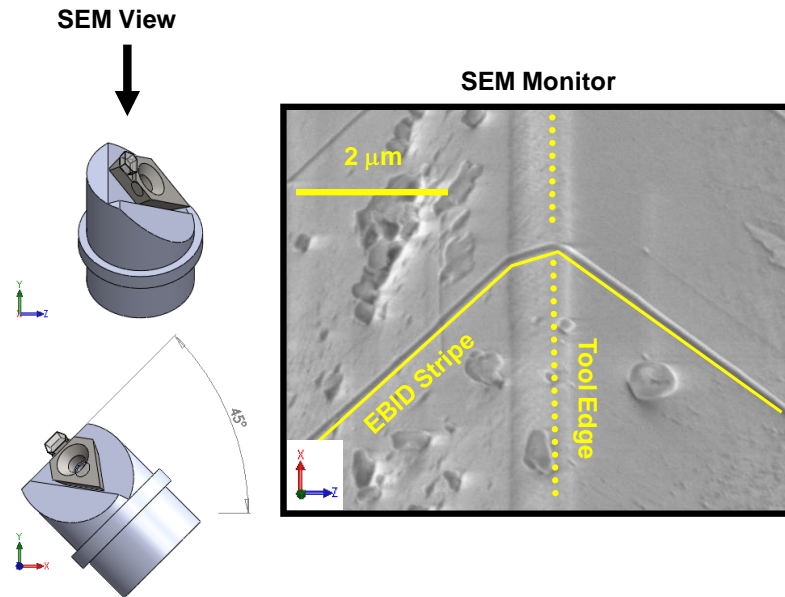


Figure 2-6: Tilting the sample 45° about Z allows tool edge pseudo-cross section to be viewed.

Images are taken of the tilted EBID stripe. The stripe outlines the worn tool edge's features, but measurements of these features cannot yet be taken since the stripe does not show the true worn tool cross-section.

2.2.1 IMAGE STRETCHING

Since the cutting edge of the tool in Figure 2-6 is tilted by a known angle (45°) away from the secondary electron detector view (plan view), the SEM and contamination stripe image is skewed vertically. If tilting angles are known, the aspect ratio of the EBID image can be adjusted so that the geometry EBID stripe matches that of the worn tool cross-section or what the worn edge would look like while looking directly down the cutting edge. This is

done without skewing the horizontal measuring scale in the SEM image. Figure 2-7 shows how a plan view image can be measured vertically from the front or side without any change to the measured length.

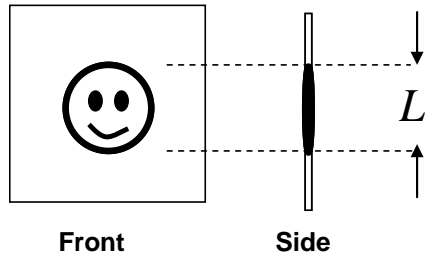


Figure 2-7: An image object will have a height L when viewed straight on or from the side

If the object in the image is pitched away from the viewing plane, the object will be “shrunk” vertically, and any measurements taken vertically will be skewed. True vertical distances that would be measurable if the image had been taken straight on, as in Figure 2-7, can be recovered by stretching the skewed image. Figure 2-8 gives a schematic of this process.

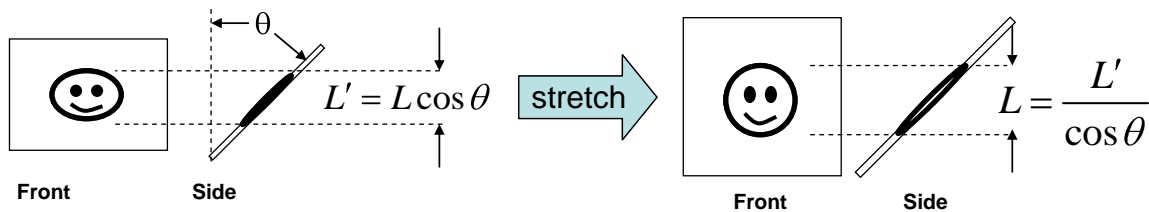


Figure 2-8: Image of a tilted object will have height L' (left). Skewing the image vertically will retain the true measurable height of the object, L .

To stretch the image to retain correct vertical distances, the image height must be multiplied by the inverse of the cosine of the angle which the object is pitched forward when the original image was taken (Figure 2-8 , left). Horizontal measurements are not affected by vertical skewing.

Images taken of tool edges with contamination stripes are taken at a pitch angle of 45°. This requires the image to be stretched vertically by a factor of 1.414. After stretching the image, the contamination stripe on the tool edge traces the profile of the tool, and measurements can be made from this stretched tool image.

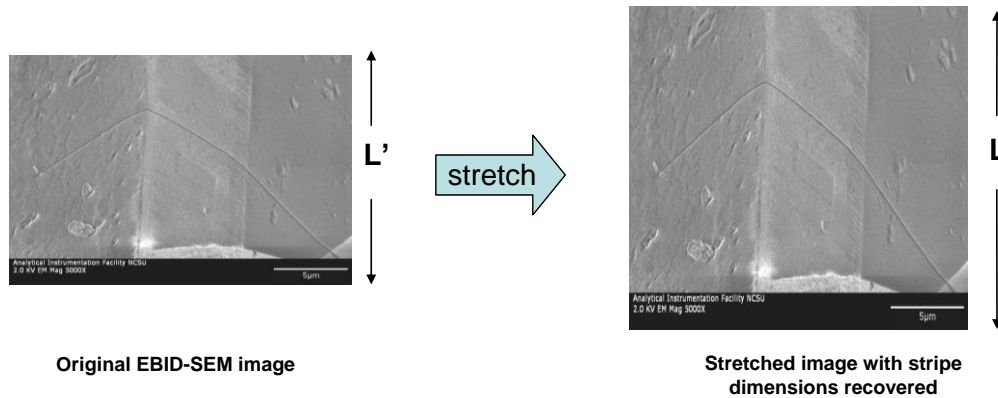
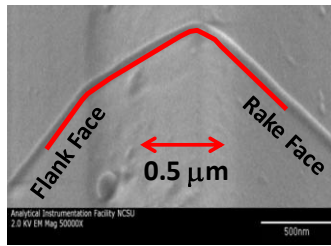


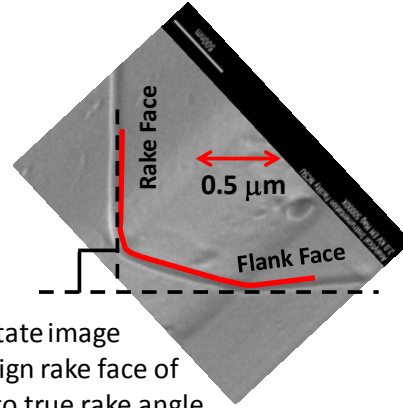
Figure 2-9: Example of SEM-EBID image being stretched vertically. EBID stripe in right image correctly traces the tool edge cross section

Since horizontal measurements are not affected by vertical skewing, the SEM image distance bar (lower right of Figure 2-9) is not affected, and can be used as a length reference.

Once the SEM-EBID image is stretched, the EBID line follows the 2D worn tool cross section viewed directly down the cutting edge. This is explained in Figure 2-10. By tracing the EBID line in photo editing software, then rotating the trace, direct measurements of the worn tool edge can be compared with 2D cutting schematics such as Figure 1-2. This allows the measured worn profile of the tool to be studied in relation to the chip formation and see the scale of the worn area with respect to depth of cut.



1.) Trace along EBID stripe with photo-editing software



2.) Rotate image and align rake face of trace to true rake angle

3.) Compare EBID trace with other worn tool cross-sections, unworn edge, depth of cut, etc. Trace outlines true 2D worn-tool cross section.

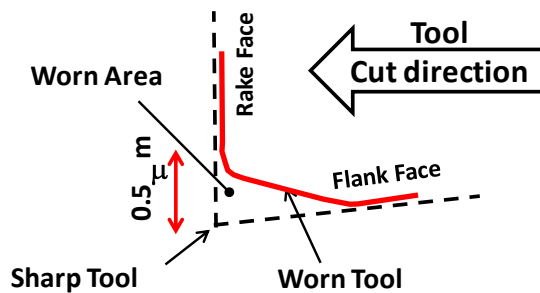


Figure 2-10: Process to recreate worn tool cross-section from EBID images.

2.2.2 STRETCHED IMAGE MEASUREMENT WITH MATLAB

Once the EBID images are appropriately stretched, there is still possibility for errors due to the subjective measurement of the image. Despite the high resolution of EBID images, the exact edge of an EBID stripe may be discerned differently from viewer to viewer. The edge of the diamond tool follows the edge of the EBID stripe on top of it, so tool edge measurements depend on the viewers definition of the exact stripe edge.

An image analysis tool called Digitize09³ was created in Matlab to alleviate subjectivity errors. Figure 2-11 shows a screen shot of two examples of an image being analyzed with Digitize09. The user uploads an EBID JPEG file into the Matlab Digitize09 function. The user

³ Digitize09 is based on the script Digitize08.m by Todd C. Patakey available at the Matlab Central File Exchange. Ken Garrard of the PEC modified the script to incorporate circle fitting algorithm and filled selection markers, and the author incorporated tool edge interpolation and area integration.

can select pixels from the stretched EBID image. Selected pixels show up as blue dots. These selected pixels can be stored as an array of XY values in the Matlab workspace. To convert pixel values to real measurements, two pixels are selected at the ends of the measure bar at the lower right of each SEM image. Taking the measure bar's value, then dividing by the difference in end-pixel X-values of the measure bar will give the scaling factor for the image.

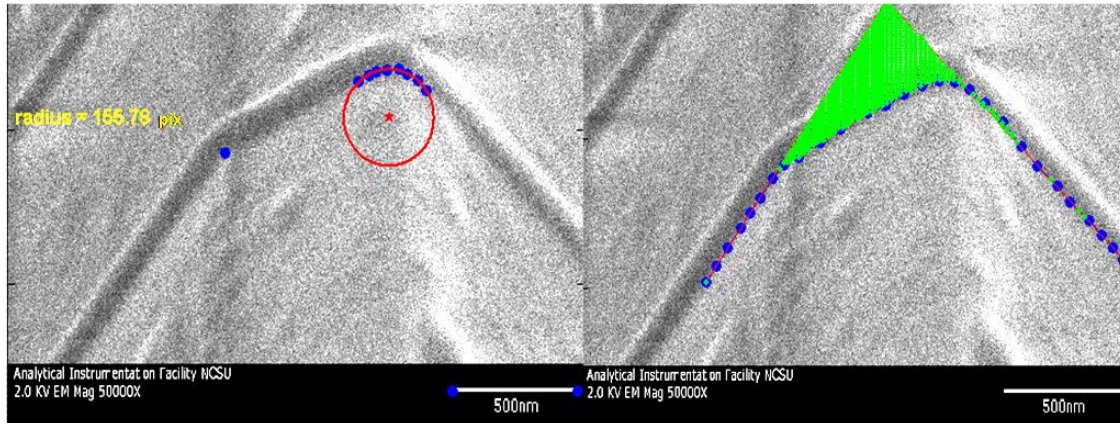


Figure 2-11: Digitize09 allows a user to select individual pixels (blue dots) along the EBID stripe. These pixels are used to calculate wear land, edge radius, and scaling (*left*) and worn area and included tool angle (*right*).

Two subroutines are available that calculate edge radius and worn area. If pixels are selected around the edge radius of the worn tool, the edge radius subroutine interpolates a circle through the selected points. It then gives the radius in terms of pixels (Figure 2-11, *left*). If pixels are selected all along the EBID stripe, the worn area subroutine will interpolate two straight lines along the rake and flank faces. The two lines and the selected edge form a closed polygon which is then integrated to find the area (green triangle in Figure 2-11, *right*). In addition, the area subroutine calculates the angle between the interpolated lines (red lines in Figure 2-11, *right*). This angle represents the included tool angle, which can be compared against the tool manufacturer's stated tool dimensions to determine how accurate the image stretching process recovers true tool edge dimensions.

2.3 WEAR LAND MEASUREMENT WITH SCANNING WHITE LIGHT INTERFEROMETER

Measuring a worn diamond tool via EBID images require an hour or more of time on the SEM depending on the ability of the user. A method for more rapid measurements is necessary for larger experiment sample spaces. A scanning white light interferometer (SWLI) can be used to measure relatively flat, reflective surfaces. The low aspect ratio of the wear land allows it to be viewed in the SWLI. This requires tilting the worn tool such that the wear land is parallel to the SWLI's viewing plane. Figure 2-12 and Figure 2-13 give examples of a diamond tool being measured by a Zygo NewView 5000 SWLI. Interference fringes will not appear unless the measured surface is close to parallel to the viewing plane. The SWLI stage can be tilted in two directions until fringes appear on the wear land region, therefore a device for repeatable mounting of the tool is unnecessary.

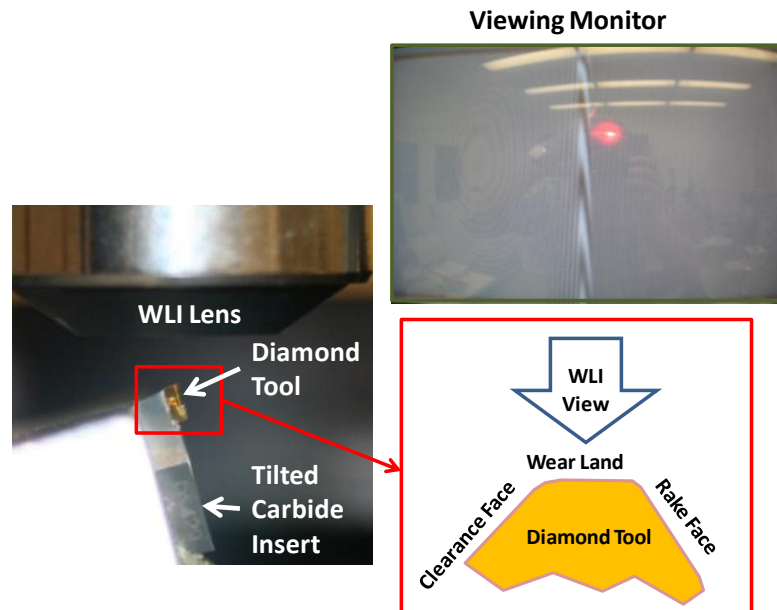


Figure 2-12: Diamond tool is tilted to allow the wear land to be measured by a SWLI (*left*). Zygo NewView monitor showing fringes along the wear land (*upper right*).

When the wear land is parallel to the SWLI viewing plane, the NewView can take a measurement using the Metropro controller software. Figure 2-13 shows screen captures

of wear land measurements. Cross-sectional slices of the surface topology are taken, and the caliper tool within the MetroPro can be used to measure the wear land length.

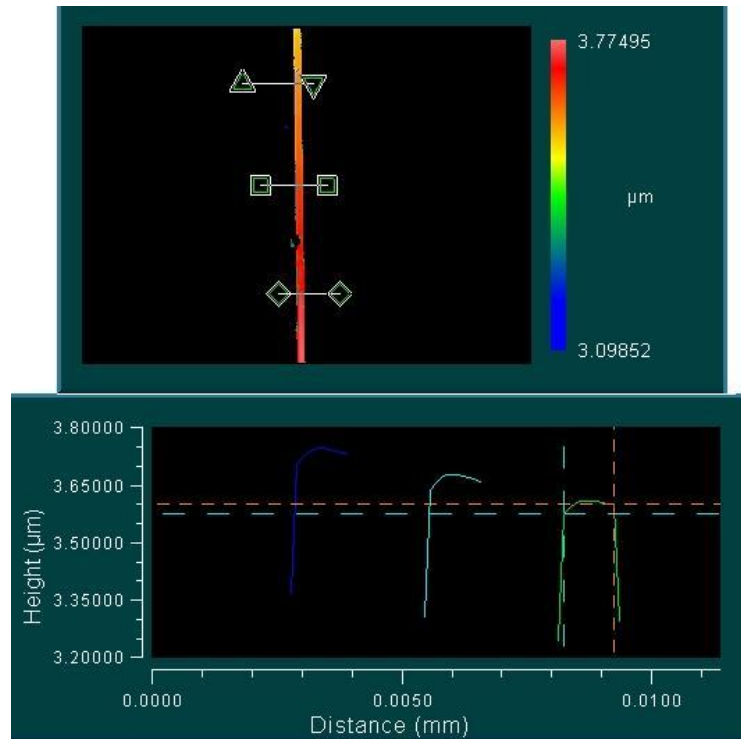


Figure 2-13: Metropro image showing a wear land being measured. Calipers on the lower image measure the top-most slice of the upper image.

The horizontal resolution of the Zygo NewView 5000 SWLI at 100x zoom is 0.01µm. Multiple slices of the surface image can be taken along the length of the tool. This allows many measurements to be statistically analyzed.

3 WEAR EXPERIMENTS MACHINING AL6061

Al 6061-T6 is an aluminum alloy commonly used in engineering applications and is diamond machinable. Prolonged machining exhibits a degradation of surface finish due to the wear of the tool. Wear is gradual and predicted to be abrasive in nature as a result of the hard alloying inclusions. Abrasive wear is commonly described using Archard's wear law [2]. This law states that the worn volume is proportional to the normal force and sliding distance. In equation form, this gives:

$$V = k \cdot F \cdot d \quad (3.1)$$

If diamond tool wear from Al6061 is abrasive in nature, it should follow Archard's wear law. Machining experiments measuring wear volume and forces are described below. Data from these experiments were used in an empirical model to determine if diamond turning of Al6061 follows Archard's wear law.

3.1 EXPERIMENTAL SETUP

The orthogonal cutting geometry is implemented in a cylindrical geometry with a narrow disk of the workpiece material as shown in Figure 3-1. Previous studies on the wear of diamond on Al6061 required cutting distances on the order of kilometers before measurable wear could be observed [5,14]. This requires a workpiece holder that can incorporate multiple, replaceable disks. The fabricated holder in Figure 3-1 consists of a thick aluminum base and cover plate that fastens the workpiece disks with four cap screws. The thick base and cover plate limits plate waviness and runout in the spindle axis direction. Axial runout of the disks was measured prior to DT using a Federal electronic indicator gauge, and resulted in magnitudes of less than 15 μm . The disks were centered on the vacuum chuck with reference to the disk perimeter edge using an electronic indicator gauge.

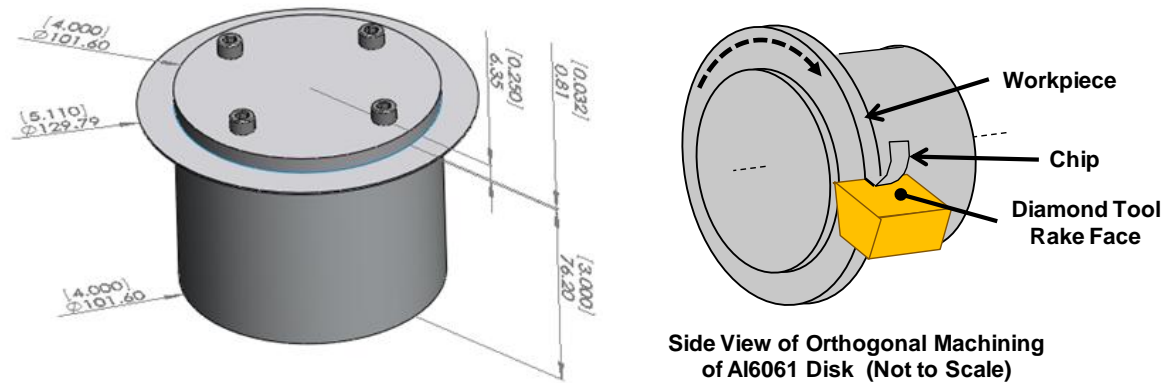


Figure 3-1: Holder dimensions for replaceable Al6061 disks (left) and setup for orthogonal cutting (right).

Table 3-1: gives cutting parameters and material properties for the Al6061-T6 abrasive wear experiments. Cutting velocity is determined from the diameter of the disk and a set spindle speed of 500 rpm. As the disk is machined, the diameter and the cutting velocity decrease. It has been shown that cutting velocity does not affect tool forces over this range [14].

Table 3-1: Material and cutting properties for abrasive wear experiments

Material	Al6061 Disk
Cutting Velocity	3.40 - 2.66 m/s
Depth of Cut, DoC	0.1-2.5 μm and 2 μm
Material Width, w	0.813 mm
Material Hardness, H	1185 MPa _a
Young's Modulus, E	70 GPa _b
Machinability	50% _{b,c}

_a Determined from Vickers microhardness test
_b Determined from [15]
_c Based on 0-100 scale of aluminum alloys

The geometry of the tool plays a significant role in the forces generated during a machining process. As the tool wears, this geometry changes as do the machining forces. To assess these changes, a force measurement system was incorporated into the tool post shown in Figure 3-2. The post allows cutting forces to be resolved along the load cell axes while maintaining the high required preload. A Kistler 9271A three-axis load cell was used. The tool holder with diamond tool on the load cell had a natural frequency greater than 20 kHz.

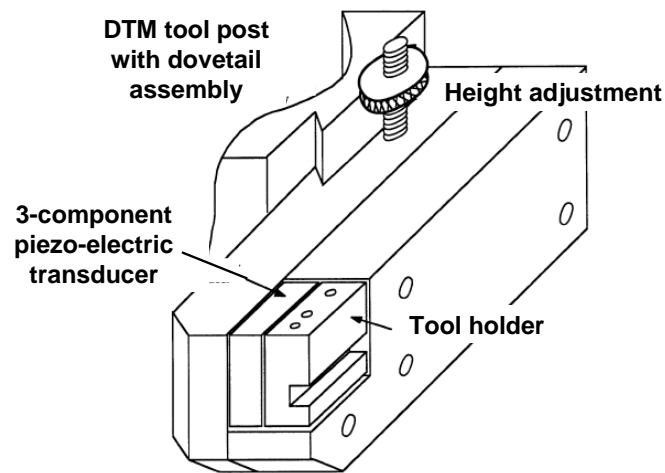


Figure 3-2: Diamond tool post incorporating a 3-axis piezoelectric load cell for dynamic force measurement [5].

Load cell charge signal was directed into a Kistler 3504 three-channel charge amplifier, and into a National Instruments SCB-88 data acquisition board. A NI Labview virtual instrument was programmed that allowed data acquisition of 1000 samples/s and forces to be monitored real-time on a virtual oscilloscope display.

Initial experiments involved cutting at several depths of cut (DoC). This was done to validate measured tool forces against previous experiments on Al6061 [5]. Chip formation on the tool may affect force signals, so an appropriate DoC that allowed chips to clear the tool was necessary. All cutting was conducted with an oil stream and compressed air directed at the cutting region. The DoC is determined by dividing the prescribed feed

velocity by the spindle speed. Large DoC's (on the order of 10 μm) created chips that built up on the tool, even while using oil and an air stream to blow them free (cutting oil is Mobilmet Omicron⁴). A depth of cut of 2 μm was found to be an appropriate DoC that allowed chips to fly clear of the diamond tool with a stream of air and oil. The tool used to turn both the Al6061 disks was a flat edge natural diamond with 2.045mm wide cutting edge, 0° rake, and 6° clearance angle supplied by Chardon Tool.

The Al6061 disks were turned on an ASG 2500 diamond turning machine, shown in Figure 3-3. Prior to cutting, the aluminum disk or steel fin was aligned with the center of the tool using a microscope. Machine axis coordinates were stored in memory so that the tool center location could be relocated with consecutive cuts. Material was initially turned with a carbide tool to reduce runout of the disk perimeter. This ensured reduced vibrations in force measurements during initial contact with material, and maintained a more accurate measure of cutting distances.



Figure 3-3: ASG-2500 diamond turning machine and control center

⁴ Mobilmet Omicron is currently discontinued, replaced by Mobilmet 426. It is a non-staining, non-corrosive oil based lubricant.

3.2 RESULTS

3.2.1 DEPTH OF CUT AFFECT ON FORCES AND CHIP FORMATION

Force signals were measured for 12 seconds around the moment the tool entered the workpiece (plunge) and exited the workpiece (backout). Figure 3-4 gives examples two such measurements for a new tool cutting Al6061 at 2.5 μm depth of cut. Forces increased rapidly after initial contact and remained steady for the duration of the cut.

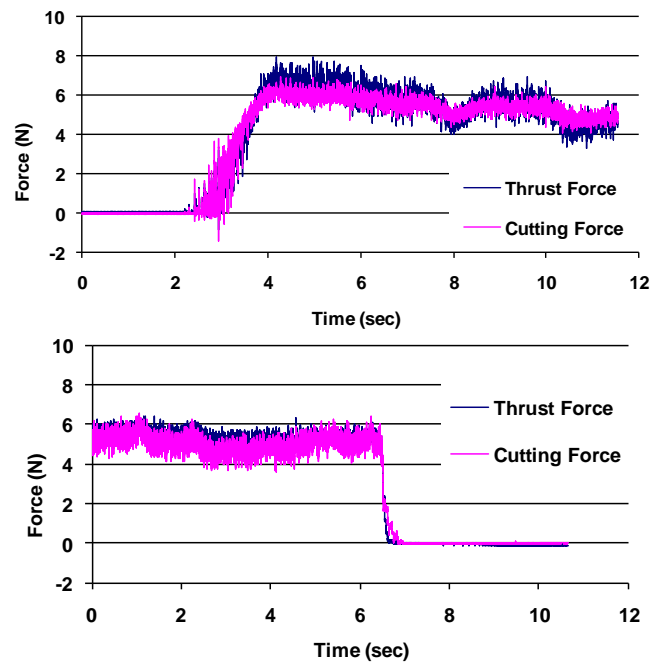


Figure 3-4: Example force measurement taken during plunge (top) and backout (bottom) during cutting Al6061 at 2.5 μm depth of cut.

Plunge and backout force measurements were averaged over 2 seconds of data to determine thrust and cutting forces for a particular DoC. Figure 3-5 gives results from the multi-DoC experiment.

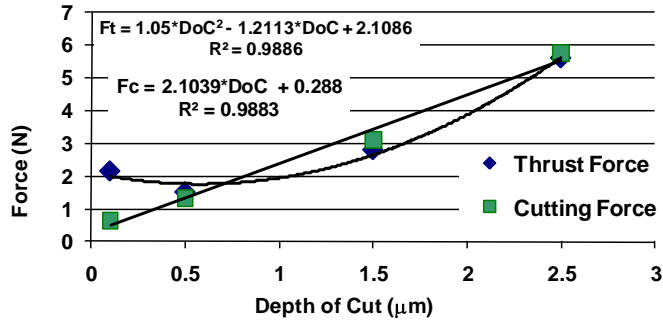


Figure 3-5: Initial cutting experiments at varying depth of cut with a sharp tool on Al6061.

Initial cutting experiments showed a linear relationship in cutting force with depth of cut. This relationship was similar to experimental results by Drescher [5], which found the slope of the cutting force to DoC line to be approximately 2.7 N/μm. This verifies the force measurement technique and calibration. At a depth of cut of 0.1 μm, the thrust force was significantly higher. This may occur when the DoC is too small for the tool to cut, and material flows under the tool (called ploughing). Chips did form during the 0.1 μm DoC experiment, though ploughing still may have occurred. Chips clustered on the tool 2.5 μm DoC experiment, shown in Figure 3-5, and not at 1.5 μm. A DoC of 2 μm was deemed appropriate for further wear experiments, so that chip accumulation would not alter measured tool forces or application of coolant.

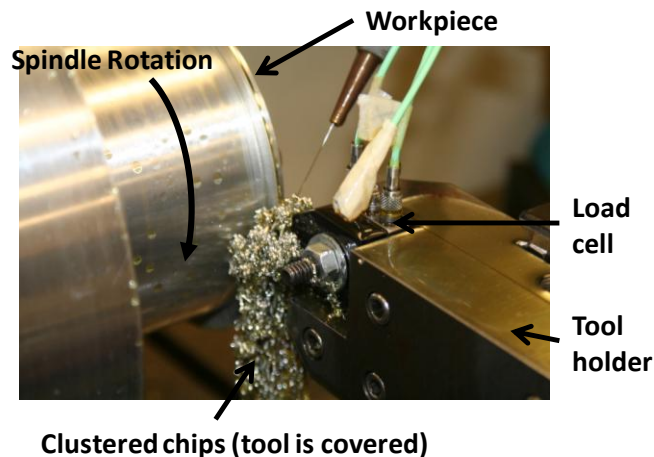


Figure 3-6: Clustered chips on the diamond tool while cutting Al6061 at 2.5 μm DoC.

3.2.2 CUTTING FORCES AT 2 μ M DOC

Plunge and backout forces were measured for cut intervals of 2.5 km distances for a total cut distance of 10 km. Figure 3-7 gives these force measurements. At 2.5 km, chips started accumulating on the tool, causing forces and force signal noise to be erroneously high. The increase in forces show how chip accumulation needs to be addressed when measuring cut forces. Both cut and thrust forces increased linearly with cut distance and subsequent tool wear.

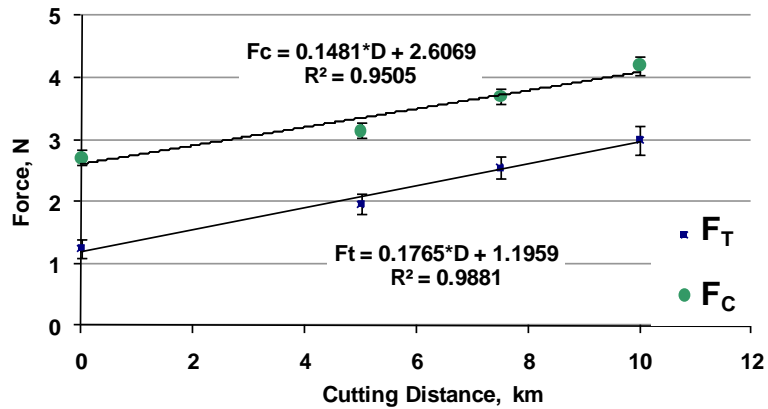


Figure 3-7: Tool forces measured while cutting Al6061. Error bars show one standard deviation.

3.2.3 TOOL WEAR MEASUREMENTS

EBID images were taken of the tool after each 2.5 km cut interval. Measurements were also taken of the sharp tool for comparison. Figure 3-8 shows three of these measurements. For each image, the left side is the flank face of the tool, and the right is the rake.

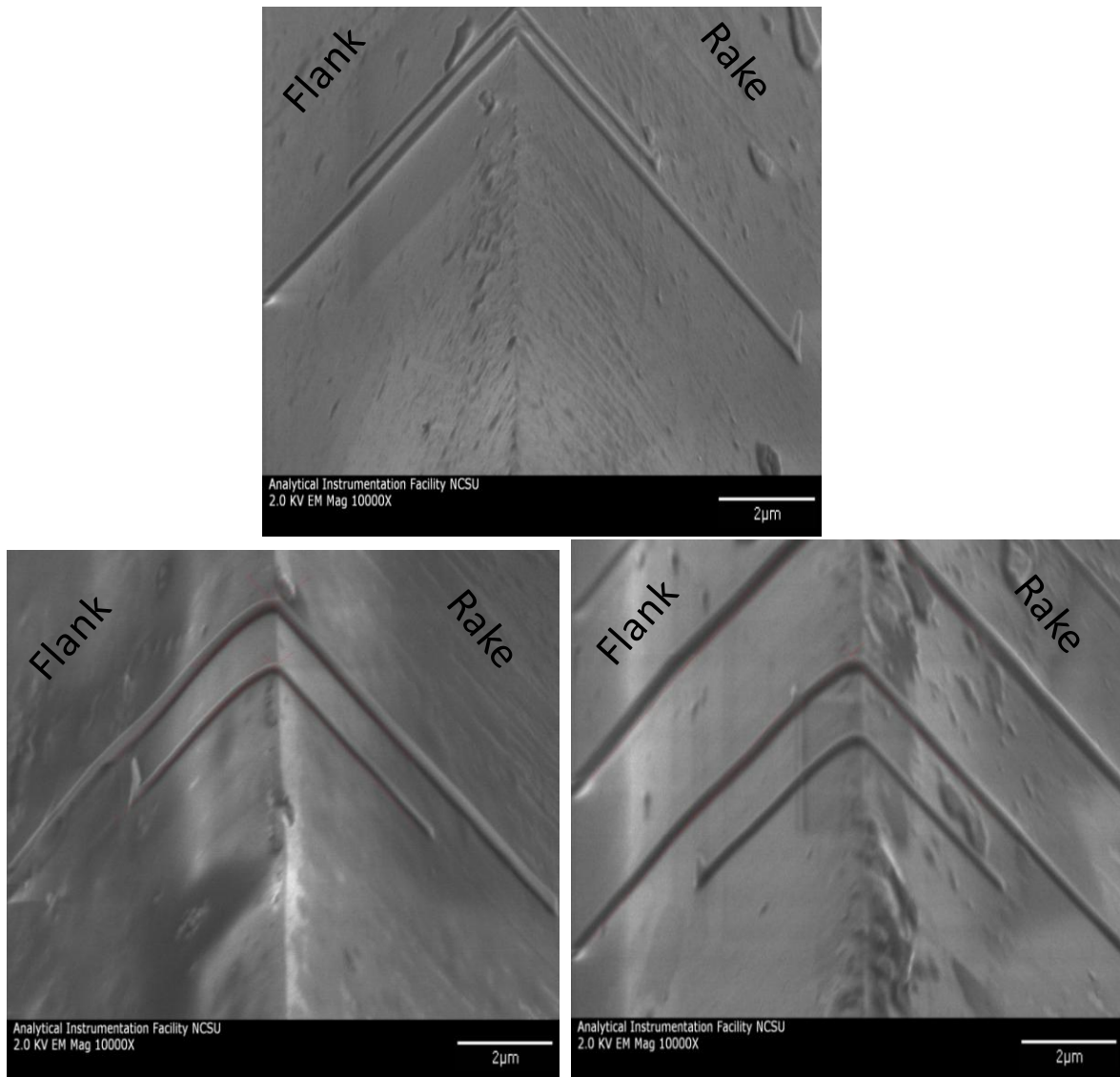


Figure 3-8: EBID image of sharp tool (top) and worn after cutting 2.5 km (lower left) and 10 km (lower right) of Al6061.

EBID images were stretched to view the worn tool cross-section. These cross-sections were traced to show the progression of tool wear for the four cut distances. Figure 3-9 shows these traces. The wear progressed with a rounding of the cutting edge, and a formation of the wear land parallel to the cut direction, and perpendicular to the rake face.

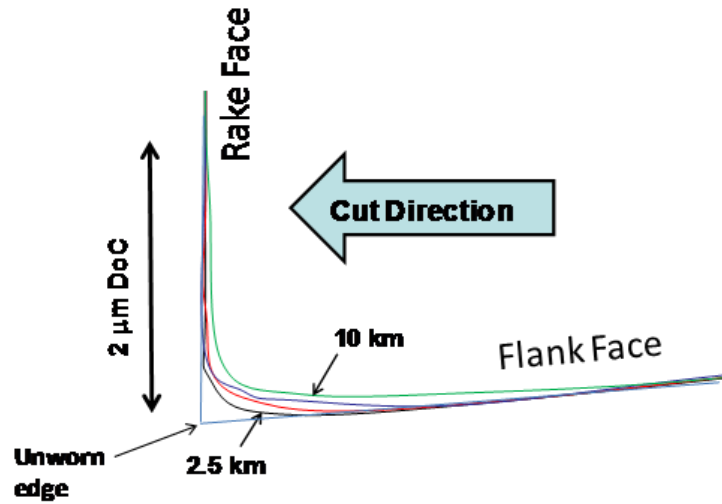


Figure 3-9: Traced EBID stripes of diamond tool after cut distances of 2.5, 5, 7.5 and 10 km cut distance on Al6061

The wear land, edge radius, and worn area were determined using the Digitize09 Matlab script. Figure 3-10 gives results for the edge radius and wear land measurements. Both features increased linearly with cut distance, implying a relationship between the wear features and forces, which also increased linearly.

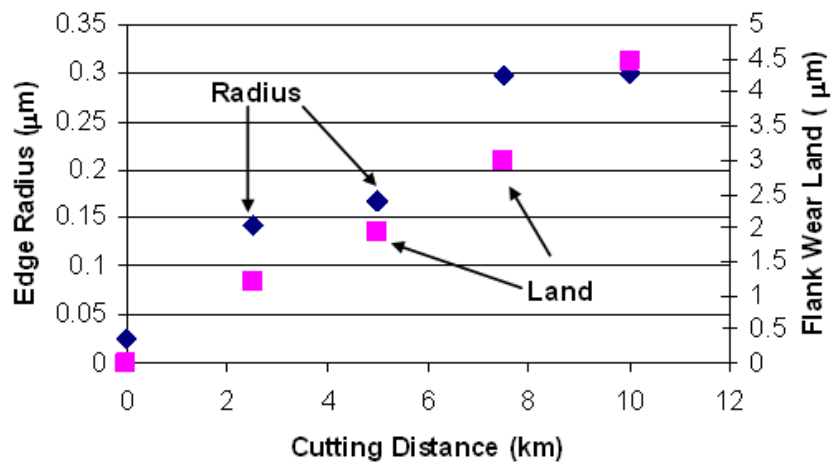


Figure 3-10: Wear geometry measured from EBID images after cutting Al6061.

The edge radius grew at a rate of approximately 30 nm/km and the wear land grew at a rate of approximately 450 nm/km. EBID images were analyzed with Digitize09. Wear areas from Digitize09 were used to determine the diamond tool wear volume by multiplying the worn area by the workpiece material width. Figure 3-11 shows the wear volume increased nonlinearly with cutting distance.

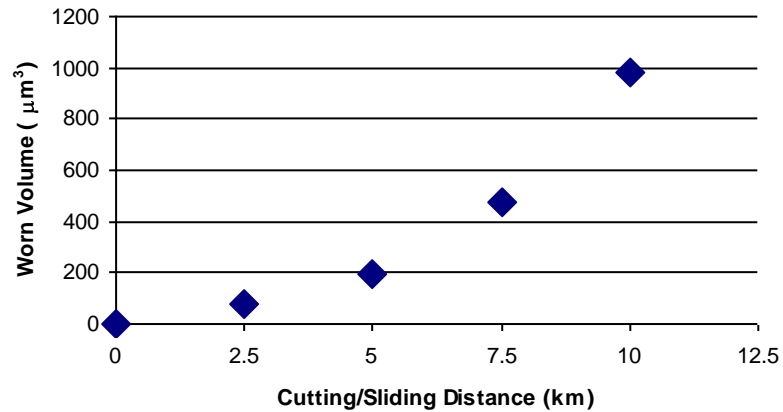


Figure 3-11: Wear volume of diamond tool cutting Al6061.

Crompton et. al. [1] observed a linear increase in worn volume with sliding distance after abrading different materials on diamond. This was done by rubbing disks of wearing materials on flat diamond surfaces, then measuring the worn volume in an interferometer microscope. Their linear results appear contrary to Figure 3-11. In their sliding wear experiments, a constant normal force was applied between the contacting test materials. The cutting process is different in that the tool-workpiece contact forces increase with increased tool wear and subsequent sliding distance, as seen in Figure 3-7. When a constant force is supplied to Archard's Equation, the volumetric loss becomes a linear function of sliding distance. If force increases with sliding distance, the volumetric loss governed by Archard's Equation will increase non-linearly with sliding distance.

3.3 DISCUSSION

The tool forces and wear geometry both increased linearly while the volumetric wear increased at an increasing rate. The increase in tool forces is presumed to be due to the change in tool edge geometry caused by wear. Before the worn volume can be coupled with the increase in tool forces, the relationship between wear geometry and tool forces needs to be addressed. Since wear geometry and tool forces both increase linearly, any relationship between the two would follow a linear trend.

The nonlinear increase in wear volume is predicted by Archard's wear equation when both force and distance factors vary. As the tool wears, a linear increase in force multiplied by a linear increase in distance would give a parabolic increase in volume. The question remains how to use the measured cutting forces and derive a measured expression for normal force, as is used in Archard's equation. The next section describes a how to acquire a normal force that can be used in Archard's equation based on observed wear geometry and a simplified model of forces acting on the tool. This model utilizes the measured tool forces and the measured wear volume to calculate the Archard wear coefficient.

4 ABRASIVE WEAR MODEL

The relationship between tool forces and wear from the Al6061 experiments may be described by Archard's wear equation as long as the normal force used in the equation increases linearly. Since the measured tool forces increase linearly (Figure 3-7), this normal force can be determined from the measured forces. Once derived, the relationship between normal force, cut distance, and wear can be supplied to Archard's equation. This can then determine if diamond tool wear when machining Al6061 is abrasive in nature, and determine a specific Archard wear constant for diamond machining of Al6061. Worn volume can then be determined for future experiments from easily measured tool forces.

4.1 ARCHARD WEAR AND WORN TOOL FORCES

EBID images of the Al6061 worn tools exhibited a wear pattern described by a flattened region called the wear land, and a rounding of the cutting edge called the nose radius. While wear does occur on the rake face of tools, the majority of volume loss occurs from the formation of these two features. Figure 4-1 shows how these features form the 2D worn area (A_w) from the unworn diamond edge. The worn surface of the diamond can be determined from EBID-SEM images, and the worn area calculated using the software techniques shown in Figure 2-11. The worn area can be multiplied by the material width (w) to determine worn volume. A simplified analysis of tool forces similar to that conceived by Arcona [6] for the initial construction of his tool force model is also shown in Figure 4-1, and is further discussed in Chapter 4.2.

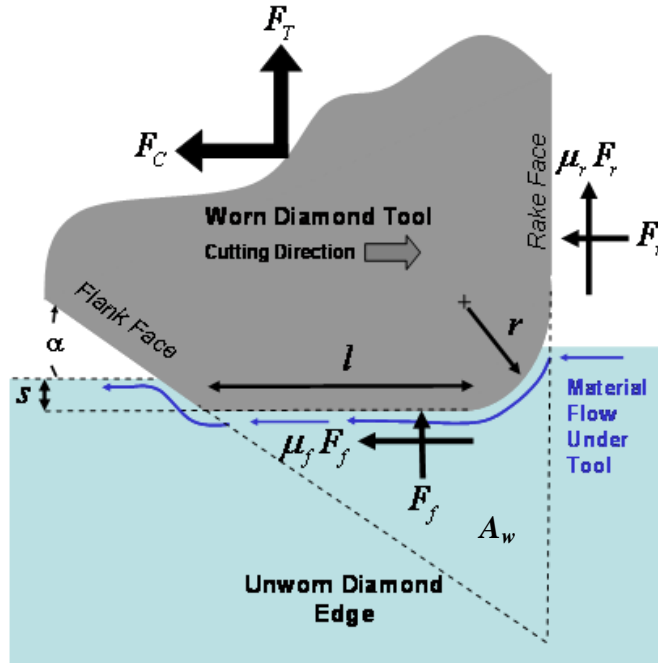


Figure 4-1: Schematic of worn diamond tool, average forces acting on the tool, and resultant tool forces.

The worn volume described by the Archard Wear Law for abrasive wear depends on sliding distance (d_s), which is the same as the cutting distance. Images of tools worn by Al6061 showed edge radii an order of magnitude smaller than wear land lengths, therefore the edge radius contributes less to the geometry of the worn volume. Since the wear on a diamond tool occurs primarily on the flank face, the average flank force (F_f) is used as the acting normal force in the Archard wear formulation.

$$V = A_w \cdot w = k \cdot F_f \cdot d_s \quad (4.1)$$

When wear studies incorporate materials of varying hardnesses, Archard's wear equation includes an inverse proportionality to the hardness of the softer of the worn materials [1,2,16]. The wear coefficient given in Equation (4.1) details the wear volume per applied load and sliding distance. Dividing by material hardness gives a coefficient related to the probability that a wear particle will be produced when surface asperities contact one

another [2]. Since only diamond is being studied, dividing by the material hardness is unnecessary.

4.2 AVERAGE FLANK FORCE

A generalization of forces acting on a worn tool with 0° rake angle are also shown in Figure 4-1, assuming different rake and flank friction coefficients, μ_r and μ_f , respectively. While studies have hypothesized various normal stress distributions on the tool edge [14,20,21], the average forces acting on the tool can be determined from forces measured during cutting experiments. Summing the forces in Figure 4-1, all generalized contacting forces on the diamond tool can be resolved into functions of the measured cutting (F_C) and thrust force (F_T) and coefficients of friction (μ_r, μ_f). The normal flank force is found in particular by Eq.(4.2).

$$F_f = \frac{F_T - \mu_r F_C}{1 - \mu_r \mu_f} \quad (4.2)$$

Arcona [14,6] developed a unique method for directly observing the chip formation process that lead to the development of a tool force model. While the task of determining the shear angle has had many attempts [17-20], Arcona's process enabled the shear angle (ϕ) for several materials to be directly measured. He also determined the coefficient of friction at the chip/rake interface as a function of the shear angle by summing the vertical forces acting on a chip segment.

$$\mu_r = \frac{\cos \phi - \frac{\sin \phi}{\sqrt{3}}}{\frac{\cos \phi}{\sqrt{3}} - \sin \phi} \quad (4.3)$$

Further cutting experiments by Arcona indicated a coefficient of friction between the diamond tool flank and workpiece (μ_f) less than that calculated with Equation(4.3). This

was attributed to observed segmented chip formation, during which the friction between the newly formed chip segment and the tool rake face intermittently approaches the higher static value. Build-up formed on the rake face during experiments also indicates adhesion, which would yield a higher coefficient of friction than sliding without adhesion. While μ_r is higher than μ_f , it can be determined from Equation (4.3), and μ_f can be determined from sliding experiments [3,14].

Equations (4.2) and (4.3), with experimentally determined μ_f , can be used to acquire the flank force (F_f). Cross section wear area (A_w) can be determined from EBID images and integration methods previously described. The worn region of the diamond tool is assumed to be the same width as the turned material. The wear area combined with the wear width (w) can determine the worn volume (V_w).

4.3 RESULTS

To determine the average flank force in Eq.(4.1), friction coefficients need to be determined. Wilks et. al. [3] describes several experiments concerning the friction of diamond on various metals. While experimental conditions varied, friction coefficients ranged between 0.1 to 0.4. Arcona [14] found a friction coefficient of diamond on Al6061 to be 0.2. Variations of μ_f in Eq. (4.2) have little effect on F_f , nevertheless a value of 0.2 is assumed for Al6061 based on Arcona's experiment. Chips collected after machining were observed in an SEM, and chip thickness was measured to be approximately 3.0 μm . According to Shaw [18], this chip thickness along with the 2 μm depth of cut would result in a shear angle of 36.5°. Arcona [14,6] directly observed that Al6061 cut with a diamond tool formed a shear angle of 40°. Using these values in Eq. (4.3) gives a range of μ_r of 0.36 to 0.43. The coefficient of friction on the rake face can also be approximated from initial cutting forces. Since no wear exists during the first cut, the majority of measured forces occur from rake normal force (F_r) and rake friction ($\mu_r F_r$). The ratio of the initial thrust

force to the initial cutting force will equal the rake friction for a perfectly sharp tool with 0° rake angle [19]. Rake friction determined this way for Al6061 yields a rake friction value μ_r of 0.46. For a true tool, initial edge radius and elastic springback in the flank region contribute to thrust forces, therefore this value is higher than the true rake friction. A compromise is made by assuming the value of 38° for ϕ and 0.4 for μ_r . Using these values, the average flank force (F_f) is determined from Eq. (4.2), and multiplied by values for corresponding cutting/sliding distance. Figure 4-2 shows the wear volume plotted against these values to determine the Archard wear constant from Eq. (4.1) for diamond on Al6061.

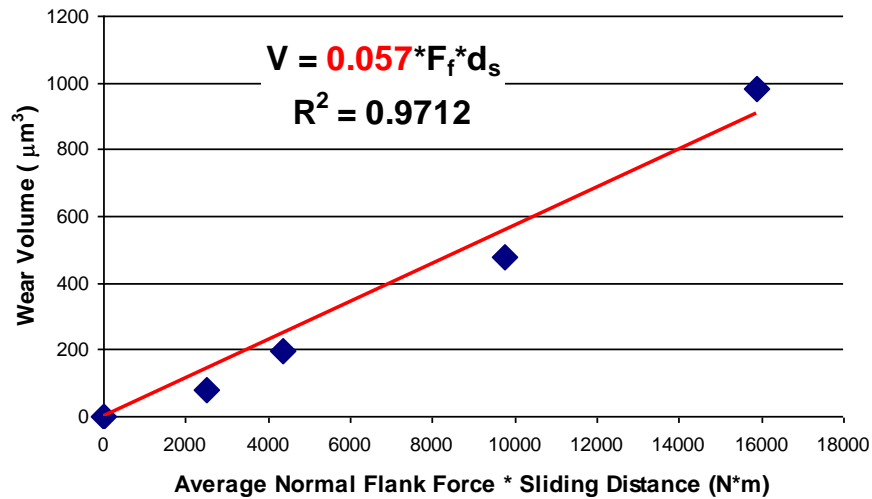


Figure 4-2: Archard wear constant determined for diamond machining of Al6061

The relationship between worn volume and normal force and sliding distance was linear, with a coefficient of determination (CoD) of 0.97. This means 97% of the variance in wear volume can be predicted from the best fit line. The slope of this line determines the Archard wear constant. For these experiments, the wear coefficient was determined to be $0.057 \mu\text{m}^3\text{N}^{-1}\text{m}^{-1}$.

4.4 DISCUSSION

The Archard coefficient diamond tool wear cutting Al6061 is very low compared to values for abrasion of metals on other metals, and even diamond on other metals. Crompton et. al. [1] determined wear coefficients of diamond on many materials. Most wear coefficients they observed for diamond were below $2.5 \mu\text{m}^3\text{N}^{-1}\text{m}^{-1}$ (diamond on carborundum) with the exception of a diamond powder bonded wheel. The lowest wear coefficient observed by Archard and Hurst [22] was $78.4 \mu\text{m}^3\text{N}^{-1}\text{m}^{-1}$ (sintered tungsten carbide on sintered tungsten carbide).

Crompton et. al. [1] determined a wear coefficient of $0.12 \mu\text{m}^3\text{N}^{-1}\text{m}^{-1}$ by rubbing a $\langle 010 \rangle$ direction on a diamond cube with an unalloyed aluminum disk. When rubbing the same $\langle 010 \rangle$ direction with a duralumin (similar to Al2024 alloy), they determined a wear coefficient of $0.93 \mu\text{m}^3\text{N}^{-1}\text{m}^{-1}$. Their wear coefficient for pure aluminum was at least twice that observed from the diamond turning of Al6061, and more than 15x that for the more similar aluminum alloy. They did note, however, that no wear was observed on the diamond until a sufficient time elapsed (called the induction period). After this time, the aluminum surfaces were visible oxidized, and they noted that this oxidation was harder than the bulk metal and may contribute to higher wear rates. Diamond cutting produces clean surfaces from the separated workpiece material that contact the tool before making contact with the atmosphere. This contact doesn't allow oxidation and likely results in lower wear coefficients than that determined by rubbing experiments conducted by Wilks et. al. [3]. In addition, the aluminum and duralumin experiments by Crompton were only conducted in the $\langle 010 \rangle$ direction, which exhibits higher rates of wear than the $\langle 110 \rangle$ direction that is 45° away on the same (001) crystal plane [3].

Experiments Wilks et. al. conducted on hardened tool steel resulted in $\langle 010 \rangle$ direction having a wear coefficient 14x higher than the $\langle 110 \rangle$, signifying that the $\langle 110 \rangle$ was more wear resistant. Chip flow along the rake face of the diamond tool used for experiments in

this thesis occurs along the $\langle 011 \rangle$ direction, which Wilks showed had higher wear resistance. Chip flow along the flank of the tool occurs along a plane tilted 6° (the clearance angle) from a (001) plane. If this plane weren't tilted 6° , the chip flow would also occur along the resistant $\langle 011 \rangle$ direction⁵. See Chapter 6.1 for a more extensive description of diamond tool crystallographic orientation. Aluminum oxide formation and abrasion along a more wear susceptible direction implies that the wear coefficients determined by Crompton et. al. ($0.12 \mu\text{m}^3\text{N}^{-1}\text{m}^{-1}$ on unalloyed aluminum) ought to be higher than the $0.057 \mu\text{m}^3\text{N}^{-1}\text{m}^{-1}$ determined in Figure 4-2.

While the clean surface interaction of diamond machining explains a low abrasive wear coefficient, this type of contact may exacerbate other types of wear. If the diamond and workpiece material are susceptible to chemical interactions, this clean surface contact may increase the rate of reaction. The chemical interaction of diamond and ferrous alloys is assumed to explain high rates of wear measured while diamond turning steels [9]. The next section describes diamond machining experiments on steel and measurements of tool wear. Results are compared to the Al6061 tool wear and supplied to a model for describing tool wear on steel as a chemical reaction opposed to an abrasive interaction.

⁵ In the diamond crystal the (100), (010), and (001) planes are identical. On this plane, the $\langle 100 \rangle$ and $\langle 010 \rangle$ directions are equivalent, while the $\langle 110 \rangle$ is different.

5 WEAR EXPERIMENTS MACHINING ST1215

5.1 EXPERIMENTAL SETUP To directly compare the wear of a diamond tool machining steel with the Al6061 worn tool, the same orthogonal cutting geometry was used. The workpiece is narrower than the diamond tool edge. Cutting experiments with 1010 steel disks were performed at a DoC of 2 μ m. Peak cutting forces were very high (>10 N) when compared to those when cutting aluminum (~1-3N) and large vibration occurred with forces going from 0 to peak. Reducing the DoC to 1 μ m reduced the forces but large vibrations persisted on the 1010 steel. Inspection of the surface of the steel disk showed intermittent contact possibly due to chip buildup on the tool.

1215 steel was selected as replacement material due to its improved machinability⁶ over 1010 steel and similar hardness to Al6061. Table 5-1 shows the material properties and cutting conditions for the St1215.

Table 5-1: Material and cutting properties for steel wear experiments.

Material	St1215 Fin
Depth of Cut, <i>DoC</i>	1 μ m
Material Width, <i>w</i>	1.20 mm
Material Hardness, <i>H</i>	1850 MPa _a
Young's Modulus, <i>E</i>	200 GPa _b
Machinability	140% _{b,c}

_a Determined from Vickers microhardness test
_b Determined from Matweb.com
_c Based on 100% machinability of AISI 1212 steel

⁶ Machinability is a mechanical property of a material given as a percentage vs. another material's machinability. It is found by tests that compile tool life, tool forces, surface finish, and chip formation [24].

St1215 was not available in sheetmetal, so fins were machined into a St1215 cylinder to create the orthogonal cutting geometry with a workpiece narrower than the tool. Figure 5-1 shows a Solidworks model of the St1215 workpiece. The DoC of $1\mu\text{m}$ was maintained to reduce high cutting forces measured after machining the St1010. The uncut chip area (DoC times material width) and material hardness are primary factors affecting tool forces. The machining of steel (1 mm by $1\mu\text{m}$ uncut chip area and 1850 MPa hardness) should yield forces within 10% of those measured machining Al6061 (0.813 mm by $2\mu\text{m}$ uncut chip area and 1200 MPa hardness). The Orientation of the fins during machining was similar to the Al6061 disks in Figure 3-1.

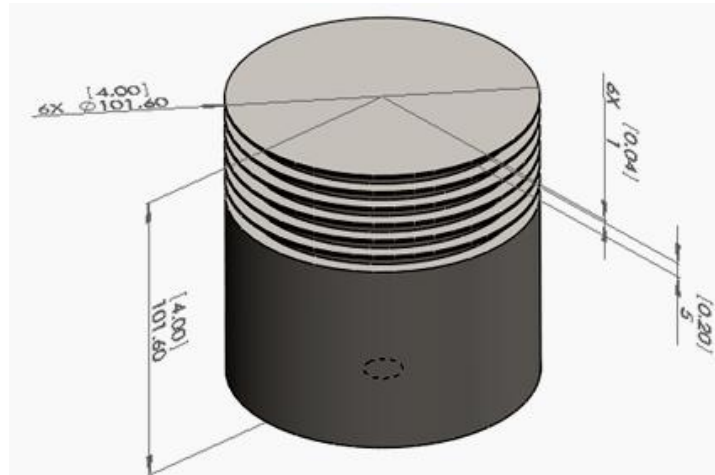


Figure 5-1: St1215 workpiece used in orthogonal turning experiments.

The same tool holder and load cell (Kistler 9271A) used in machining Al6061 were used while machining St1215. The same tool (2.045 mm wide, straight edge synthetic diamond with 6° clearance) used for the abrasive wear experiments was used in the chemical wear experiments after it was relapped by Chardon Tool. Radial runout of the disk was reduced by using a Federal gauge and tapping the workpiece into place. The steel disk was then turned with a straight carbide tool to reduce runout less than $0.5\mu\text{m}$. As with the Al6061 disks, the steel fin was aligned with the center of the tool in the Z direction, and coordinates were stored in the DTM.

Touchoff was accomplished at the desired machining speed while utilizing a machinist's microscope to see the onset of chip formation. Since aggressive wearing at small distances was expected, a microstepping program was used on the ASG9000 diamond turning machining to move the tool towards the workpiece at 100nm increments at a feedrate of 0.5 mm/min. Force measurement was initialized via signal triggering in dSpace at force values greater than 0.2 N. This triggering was used to determine successful touchoff. Utilizing the microstep program and force triggering ensures minimal tool/workpiece contact. Despite these precautions, initial wear of the tool is inevitable during touchoff.

After each cut, the tool was cleaned in a vibratory cleaner with de-ionized water and mild detergent for 5 minutes to remove any machine oil. The tool was rinsed again with water and dried with compressed air. A small drop of 5 wt% nitric acid was placed on the tool to remove any material buildup deposited during cutting. The nitric acid solution was allowed to sit on the tool for 5 minutes. The tool was once again rinsed with de-ionized water, dried with compressed air, and carefully brushed with an optical wipe saturated with acetone. After cleaning, the tool wear land was measured using a SWLI and/or EBID techniques (See Chapter 2) before being returned for another of the consecutive cuts.

Three experiment sets were conducted at three different cut speeds. The first set was conducted at 2.12 m/s cut speed and EBID measurements were taken at 5, 10, 15 and 20 meters of cutting distance. These EBID measurements are used to observe the worn tool cross-section, and the cross-section change with cut distance. The next two sets were conducted at half and twice that speed (1.06 and 4.24 m/s) for various cut distances. EBID images were taken after the first and last cut, and SWLI wear land measurements were taken after each cut. The 1 and 4 m/s cut speed experiment sets are used to observe the change in wear rate with machining speed.

5.2 RESULTS

5.2.1 TOOL FORCES

As with the experiments on Al6061, plunge and backout forces were measured after consecutive cuts at 2.12 m/s cut speed. Figure 5-2 gives these force measurements. Forces increased quickly then changed little for subsequent cuts. This is in contrast to Figure 3-7, where tool forces increased with subsequent cutting.

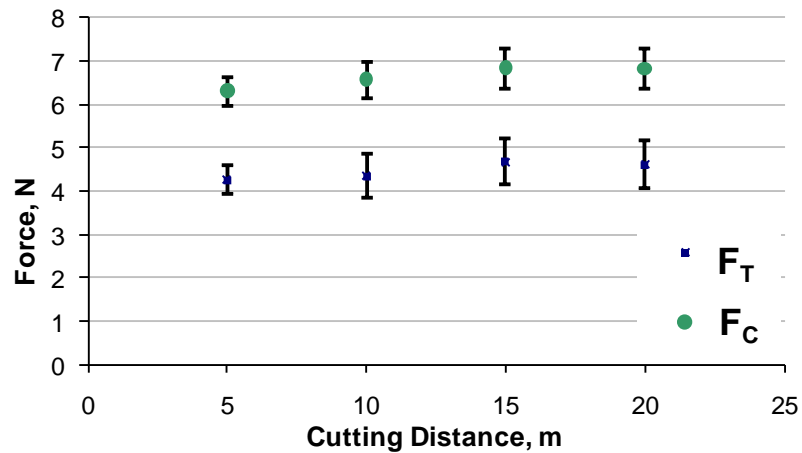


Figure 5-2: Cutting and thrust forces measured during 2.12 m/s cut experiments on St1215. Error bars show one standard deviation.

Measurement of forces during 1.06 and 4.24 m/s cut speeds were similar to that at 2.12 m/s, showing an invariance to cut speed over that range. Forces increased sharply, then remained steady for subsequent cuts. After approximately 80 m of cutting at 1.06 m/s, the tool started chattering and the continuous chip formation changed to discrete chips. Force signal noise increased abruptly, accompanied by noticeable vibration noise. Figure 5-3 shows the force signal during the onset of chattering. Cutting beyond 180 m at 4.24 m/s also resulted in chattering.

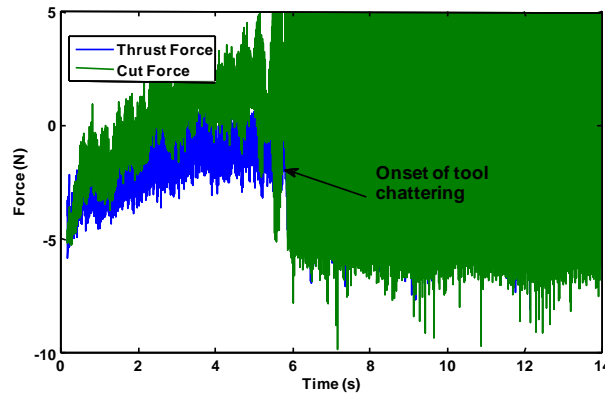


Figure 5-3: Cutting force signal as tool chattering developed. Chattering started at approximately 80 m of cutting at 1.06 m/s.

Tool forces measured for the 1.06 and 4.24 m/s cut speeds did not change with machining speed or distance. Figure 5-4 gives average measured forces. Cutting forces, F_c , for both the 1.06 m/s experiment and the 4.24 m/s experiments were approximately 7 N. Thrust forces, F_t , were approximately 4 N for both speeds. Force signal noise was slightly higher for the lower speed experiments, with standard deviations at approximately twice that of the high speed. The higher noise may be a precursor to the tool chattering seen in the low speed experiment.

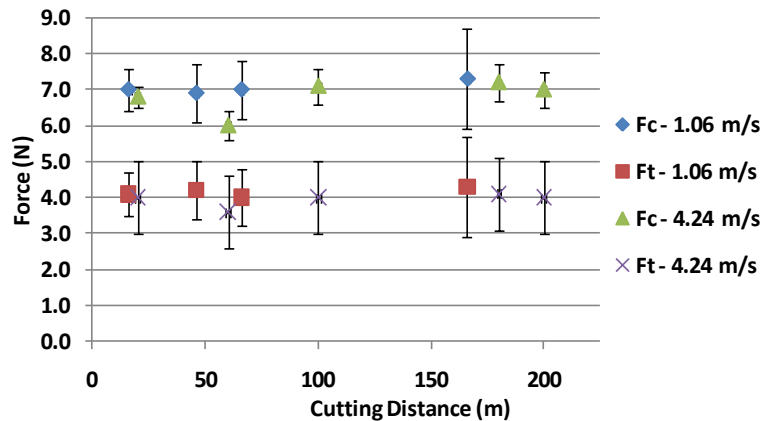


Figure 5-4: Measured tool forces for 1.06 and 4.24 m/s machining speeds on St1215. Error bars show one standard deviation.

5.2.2 EBID WORN TOOL MEASUREMENTS FROM 2.12 M/S EXPERIMENT

EBID images were taken after cutting 5, 10, 15, and 20m of St1215 at 2.12 m/s. Figure 5-5 shows two examples of these images. EBID images were also measured to determine wear land length, and worn tool volume using the Digitize09 Matlab script. EBID images were taken after several cuts at 1.06 m/s and 4.24 m/s to compare with SWLI wear land measurements, which were taken after each cut. Two examples of EBID images taken from the 2.12 m/s experiments are shown in Figure 5-5. Initial inspection revealed a substantial amount of wear at only 5 m cut distance, and a wear pattern that appeared different than that of A16061.

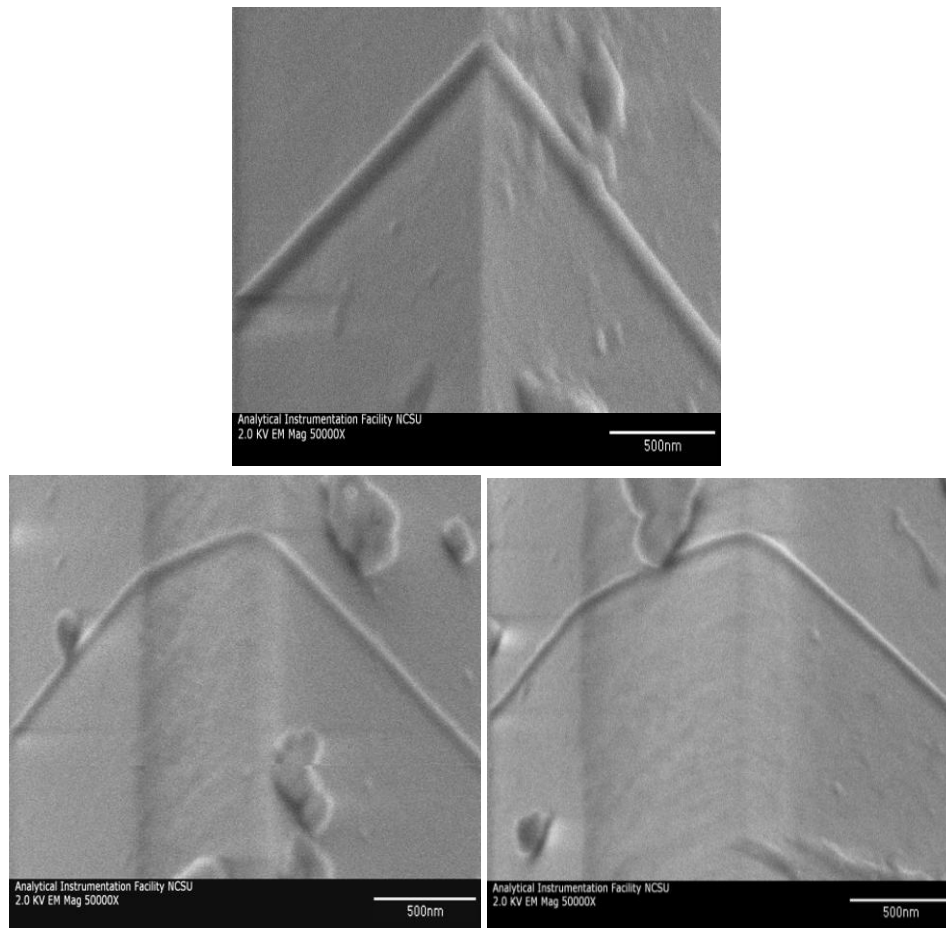


Figure 5-5: EBID image of sharp tool (top) and tool worn after cutting 5m (lower left) and 20m (lower right) of St1215 steel at 2.12 m/s.

Wear land and edge radius measurements were taken from stretched EBID images of the tool after each cut at 2.12 m/s. Figure 5-6 shows the results from these measurements. As did the measured tool forces, wear geometry increased substantially after only 5 m cut distance. With further cutting, the wear land and edge radius increased linearly.

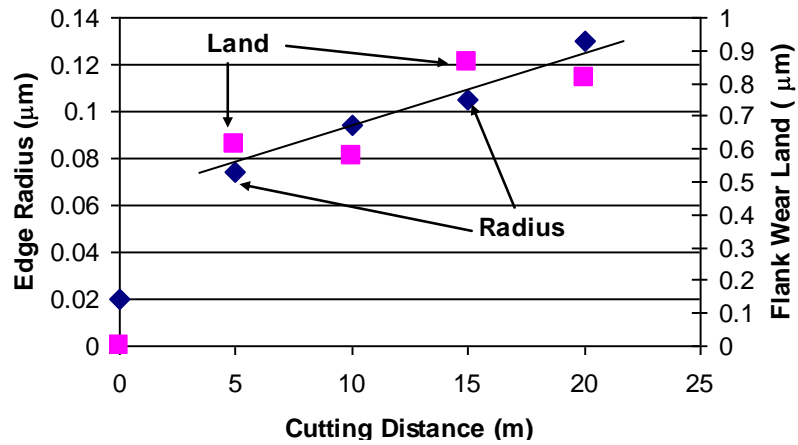


Figure 5-6: Edge radius and wear land measurements made from EBID images of tool worn after cutting St1215

Worn volume was also determined by using the Matlab script Digitize09. The results are shown in Figure 5-7.

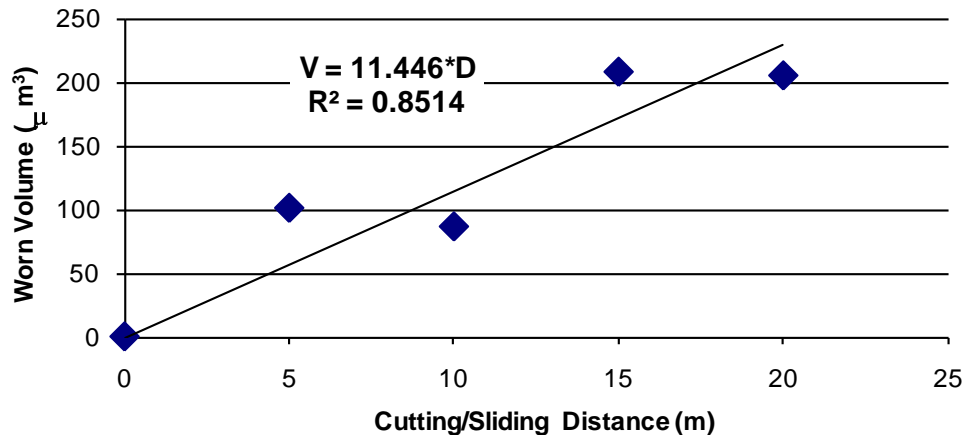


Figure 5-7: Worn volume determined from Digitize09 EBID image analysis of tool worn after cutting St1215 at 2.12 m/s.

The worn volume at 10 m was calculated to be less than that at 5 m, which is counterintuitive. This may be the result of EBID stripes made at different locations along the tool edge after each cut. EBID stripes taken near the edge of the worn region will show a lesser degree of wear. This likely occurred after cutting 10 m.

As with the Al6061 worn tool, EBID images of successive wear can be traced to show the worn tool profiles. Figure 5-8 shows the 4 successive worn tool profiles. The wear land was not parallel with the cutting direction, but rather, formed a 20° angle and remained the same with increased wear.

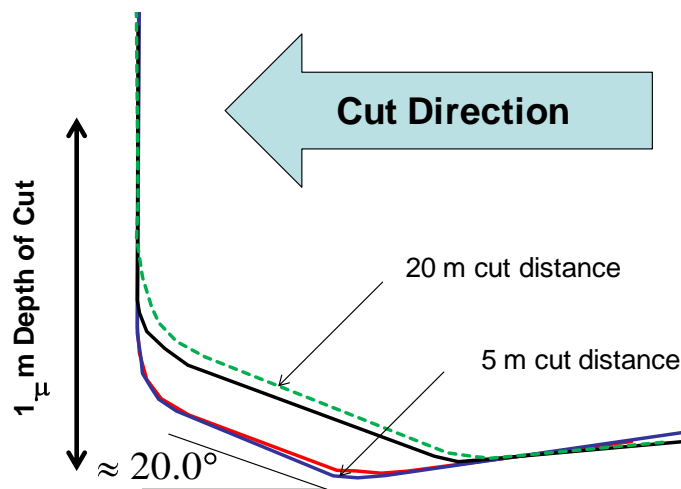


Figure 5-8: Traced EBID stripes of diamond tool after cut distances of 5, 10, 15 and 20 m cut distance on St1215.

The 20° upturned wear land was observed on all EBID images of steel-worn tools. The 20° did not change with further cut distance or with different cut speeds. The wear land receded without changing the angle it formed with respect to the rake face and cut direction.

Figure 5-9 shows the St1215 worn tool profile compared to the Al6061 taken from stretched EBID images. The tool edge geometry is greatly different for the two workpiece materials, as is the degree of wear with respect to machining distance. These differences are most

likely a result of the different workpiece materials rather than different depth of cut. The same diamond tool was used to turn both materials (after being relapped by the manufacturer) and was mounted in the same tool holder, therefore the different wear pattern cannot be attributed to the tool used or its alignment in the diamond turning.



Figure 5-9: Traced EBID stripes of St1215 and Al6061 worn tools. Tool wear profile for St1215 worn tool exhibits an upturned wear land compared to Al6061-worn tool.

5.2.3 1.06 AND 4.24 M/S SWLI WEAR LAND MEASUREMENTS

Two cut experiments were conducted to measure the variation of wear with respect to cut speed. After each cut, the tool wear land was measured in the Zygo NewView 5000 scanning white light interferometer. Nine wear land measurements were taken after each cut; 3 locations along the tool edge and 3 surface profile measurements per location.

Figure 5-10 shows the wear land data vs. cut distance. The wear land lengths were approximately the same at the same sliding distance for the different machining speeds.

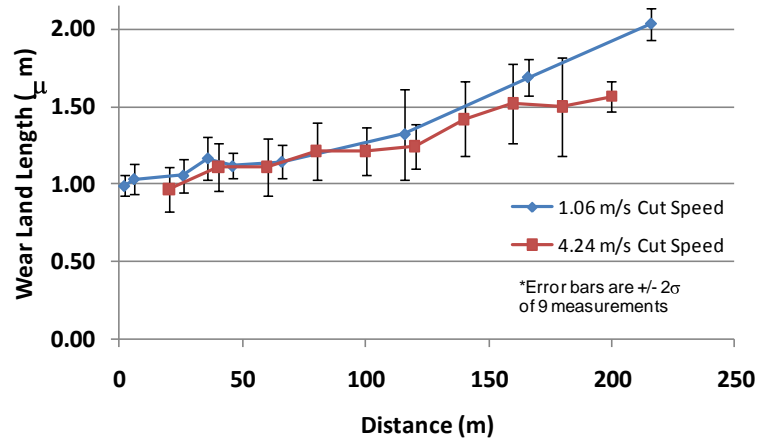


Figure 5-10: Measured wear land length vs. cut distance after cutting St1215 at two cutting velocities.

Although the wear land and was invariant with machining speed when compared to sliding distance, a comparison with machining time exhibits a difference. The tool wear caused by machining steel is expected to be chemical in nature [1,3,7-9], therefore the loss in diamond volume will occur as a reaction rate dependant on time. Figure 5-11 shows the wear land measurements compared with machining time. Chattering occurred for the last three samples points of the 1.06 m/s experiment set (at about 80 m cut distance based on a change in measured tool force signal), therefore these are omitted from wear rate calculations since a different cutting condition occurred. When compared against machining time, the wear land measurements exhibit significantly different growth rates.

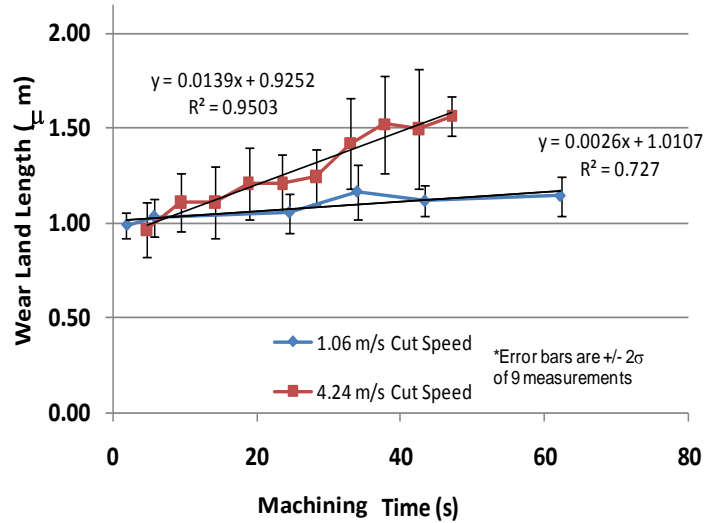


Figure 5-11: Measured wear land length vs. machining time after cutting St 1215 at two cutting velocities. The last three data points of the 1.06 m/s are removed due to tool chattering.

The volumetric wear rate is a characteristic that can be attributed to the supposed chemical reaction that occurs while cutting ferrous materials with diamond. Although the wear land increases with worn volume, it cannot directly determine the wear volume. To determine volumetric wear rates from SWLI wear land data, EBID measurements were made at the beginning and end of the 1.06 and 4.24 m/s experiment sets. These EBID measurements can be used to approximate the worn volumes and volumetric wear rates.

5.2.4 WORN VOLUME DETERMINED FROM SWLI WEAR LAND MEASUREMENTS

The EBID measurement technique allows more accurate and repeatable measurements of worn volume. By comparing SWLI wear land measurements and EBID worn volume measurements for the same tools, a transfer function can be created to convert between the two.

A relationship between SWLI wear land measurements and EBID wear land measurements can be made. Figure 5-12 shows this comparison. This correlation only depends on the respective measurement techniques and can be used for wear land measurements of tools

worn by any material, as long as the wear land is observable in the SWLI. The transfer function, F1 in Figure 5-12, can be used to convert SWLI wear land measurements into equivalent EBID wear land measurements.

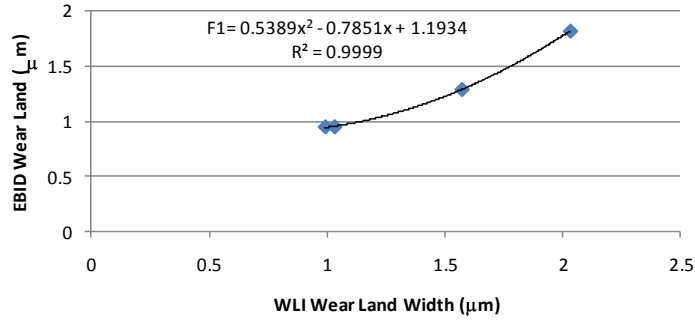


Figure 5-12: Transfer function determined that converts SWLI wear land measurements to equivalent EBID wear land measurements.

A relationship between EBID wear land length and EBID worn area needs to be determined. Table 5-2 and Figure 5-13 give EBID wear and worn area values for the three machining speed experiment data sets. Figure 5-13 shows another transfer function, F2, for converting EBID wear land into an EBID worn area. Since this function depends on the worn tool shape, it is only valid for the St1215 worn tools, which had a different worn tool profile than the Al6061.

Table 5-2: Experimental values used to determine EBID wear land to EBID worn area transfer function

Cut Dist	Cut Speed	Material	EBID Wear Land (μm)	EBID Area (μm^2)
5m	2 m/s	St1215	0.61	0.09
10m	2 m/s	St1215	0.54	0.09
15m	2 m/s	St1215	0.87	0.16
20m	2 m/s	St1215	0.88	0.19
2m	1 m/s	St1215	0.95	0.179
4m	1 m/s	St1215	0.95	0.171
216m	1 m/s	St1215	1.82	1.037
200m	4 m/s	St1215	1.29	0.46

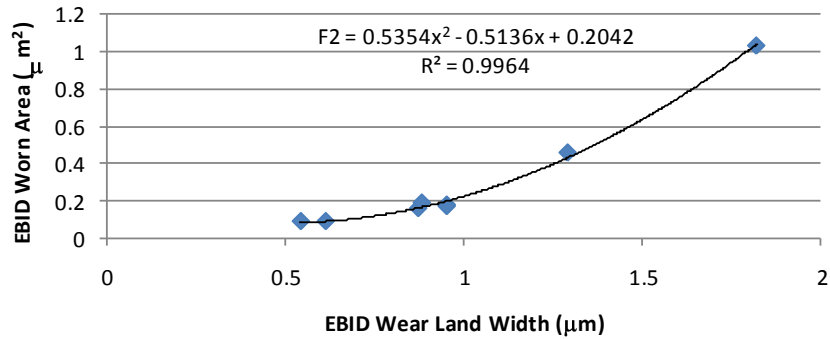


Figure 5-13: Transfer function determined that converts EBID wear land measurements to equivalent EBID worn area for diamond tools worn by St1215 in this study

The SWLI wear land measurements are supplied to the transfer function in Figure 5-12 to create equivalent EBID wear land lengths, then supplied to the transfer function in Figure 5-13 to convert to equivalent worn areas. To examine the error incurred in this process, the worn area using the transfer functions is compared to the known EBID worn area in Table 5-3.

Table 5-3: Comparison of measured EBID worn areas to worn areas determined from applying transfer functions to wear lands measured via SWLI.

Cut Distance (m)	Mean WLI Wear Land (μm)	EBID Wear Land (μm)	Equivalent EBID Wear Land from WLI Wear Land (μm)	EBID Area (μm^2)	Equivalent WLI Area (μm^2)	Land Error	Area Error
1	0.99	0.95	0.943	0.179	0.196	0.72%	9.5%
4	1.03	0.95	0.955	0.171	0.202	0.55%	18.2%
216	2.03	1.82	1.816	1.037	1.037	0.19%	0.0%
200	1.57	1.29	1.287	0.46	0.430	0.26%	6.6%

The SWLI wear land to EBID wear volume process incurs errors of less than 20%. Each SWLI wear land measurement is converted to the equivalent worn area, then multiplied by the workpiece width (1.2mm for the St1215 fins) to get worn volume.

Figure 5-14 shows these values compared with cut time for the 1.06 and 4.24 m/s experiment sets. The slope of the least-squares linear approximation gives the worn

volumetric rate. Since wear occurs immediately after cutting St1215, the linear approximations have a y-intercept. The rates determined from the linear approximation slopes represent a steady-state volumetric wear rate after initial wear, and before tool chattering occurs.

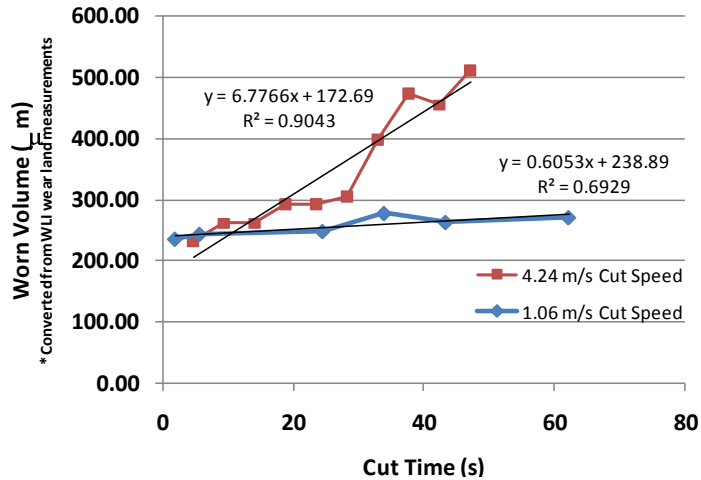


Figure 5-14: Wear land measurements converted to equivalent EBID worn volume vs. cut time.

5.3 CONCLUSIONS

Initial cutting experiments on 1010 steel resulted in excessive vibration of the tool and discrete chip formation. St1215 was chosen as a workpiece material due to its reported increase in machinability. This material allowed continuous chip formation, although chattering initiated at approximately 80 m at 1.06 m/s cut speed.

Tool wear after cutting St1215 exhibits geometry far different than Al6061. Comparable wear volumes were seen at cut distances 1000x less than that for Al6061. This higher degree of wear is not related to content of abrasive particles in the St1215 and Al6061. Shi [23] used digital images from an optical microscope to compare size and densities of hard alloying particles in the St1215 and Al6061 used in this thesis. She found the area fraction of hard particles in St1215 to be 1.2% with an average particle size of $21 \mu\text{m}^2$, compared to 3% and $44 \mu\text{m}^2$ for Al6061. The larger and more numerous particles in Al6061 indicated

that it should wear a tool by abrasion more aggressively than steel. Though the Al6061 contains higher density and larger particles, the wear from the steel was far more aggressive and indicates a wearing mechanism other than abrasion. Wear measurements of the tool taken after as little as 1 m of cutting showed that most the wear occurred within this time period. This most likely occurs during the tool touchoff.

The wear land on the tool used to machine St1215 occurred at an angle to the machining direction. This angle did not change with machining distance or speed. Wear land measurements showed that the same wear occurs at the same distance for different speeds, but varied when compared against time.

Wear land measurements taken from the SWLI to be converted to worn volume. This was done by comparing SWLI and the more accurate EBID data and creating transfer functions to convert SWLI wear land lengths to equivalent EBID wear land lengths, then to equivalent EBID worn areas. This process creates worn area data that that is less than 20% different than the worn area measured by the EBID process. This enables wear measurements to be made with the SWLI quicker than EBID without incurring too much error. SWLI wear land measurements were converted to worn areas and multiplied by workpiece material width to get worn volume. This showed the 4.24 m/s tool incurred a volumetric wear rate 10x greater than the 1.06 m/s tool

6 CRYSTALLOGRAPHIC AFFECTS OF DIAMOND MACHINING

Cutting experiments on 1215 steel yielded a wear land that was different than that observed on diamond tools used to machine Al6061. One explanation may be that different wear rates had occurred due to the different crystallographic orientations of the rake and flank face of the tool. Previous research into directional affects on the friction and wear of diamond found that small changes in sliding direction and/or orientation of the surface could have a large effect on the rate of wear [3]. The relative wear rates of the different diamond crystal planes are reviewed for a possible explanation of the different wear land.

6.1 CRYSTAL ORIENTATION OF DIAMOND CUTTING TOOLS

Like all other crystalline solids, the atoms in diamond occur in repeated patterns with multiple planes and directions of symmetry. Each carbon atom in diamond is bonded to four other carbon atoms, with each bond spaced symmetrically around the centered atom. This symmetry causes each bond to form an angle of approximately 109.5° with the three other bonds for a given centered atom.

Figure 6-1 shows a cubic section of a diamond lattice. These cubic diamond sections can be “stacked” to form the bulk diamond crystal lattice. All atoms in this cubic model are carbon atoms, with red (darker) indicating atoms within the body of the cube, and white (lighter) indicating atoms that intersect the surfaces.

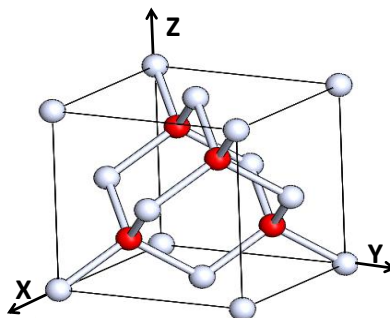


Figure 6-1: Model of a cubic element of the diamond lattice.

The x,y and z axes of this cube (and each “stacked” cube in the crystal lattice) align with the (100), (010), and (001) Miller indices planes and $\langle 100 \rangle$, $\langle 010 \rangle$, and $\langle 001 \rangle$ indices directions. Close observation of Figure 6-1 shows that each face of the cube is equivalent to the others with respect to the number and pattern of atoms intersecting the face. Each of these planes can thus be regarded as being the same plane. In the following assumption, cubic diamond planes are referred to as the (001) planes, as shown in Figure 6-2. This is commonly referred to as the (001) family of planes, or cubic family of planes. Other plane families exist for diamond, with even more directions of symmetry than the (001) family of cubic planes, but are not discussed here.

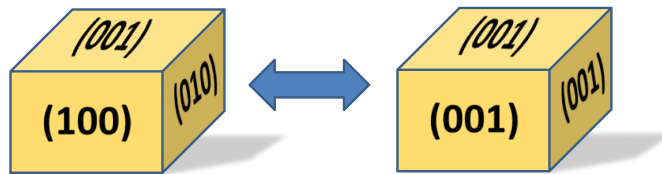


Figure 6-2: Cubic diamond planes are geometrically equivalent and can all be noted as (001) planes

Apart from planar symmetries, directions occurring on each plane may be symmetric. Taking the same (001) family of planes, there two sets of directional symmetry on each plane. Figure 6-3 shows these two sets of symmetric directions with respect to the cubic planes. From here on these labeled as either the $\langle 100 \rangle$ or $\langle 110 \rangle$ directions. There are many more directions of symmetry on the other planar families of the diamond lattice, but are not discussed in detail here.

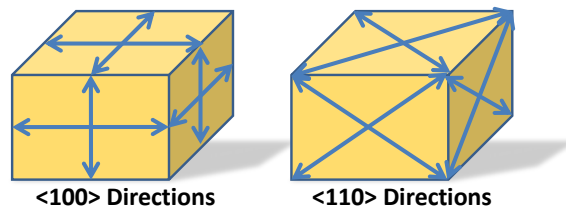


Figure 6-3: Directional symmetries on the (001) family of planes in the diamond crystal lattice: $\langle 100 \rangle$ directions (left) and $\langle 110 \rangle$ directions

Single crystal diamond tools are typically manufactured so that rake face is either a (011) or (001) plane. For a (001) rake face tool, another (001) plane is lapped so that it forms an angle (the clearance angle) from the original (001) plane, forming the flank face of the tool. Figure 6-4 shows how this may occur on the cubic section shown in Figure 6-2 and Figure 6-3. The (001) plane is lapped in one $\langle 100 \rangle$ direction so that it is pitched about the other $\langle 100 \rangle$ direction on the same plane. The new surface is no longer parallel to the (001) crystal plane.

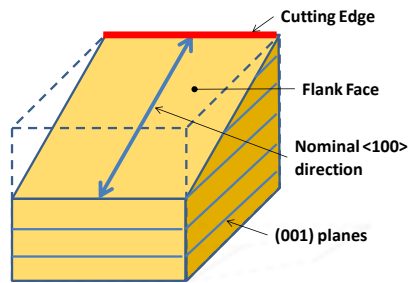


Figure 6-4: A (001) plane lapped to form a flank face of a cutting tool.

Figure 6-4 can be reoriented to show the geometry of the cutting tool with respect to the flank face created from the (001) plane, as shown in Figure 6-5. If the flank face is formed as mentioned above, the rake face will be parallel to another (001) plane. Since the clearance angle is defined as 90° minus the angle between the rake and flank face (the included angle), the clearance angle is equal to the angle between the flank face and the (001) plane.

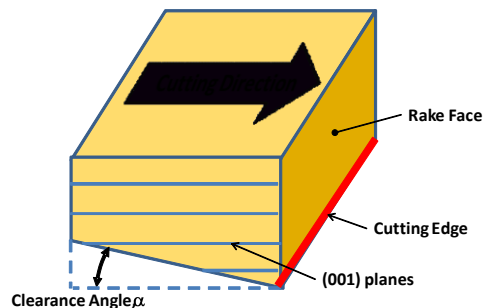


Figure 6-5: Reoriented crystal from Figure 6-4 showing relationship to cutting tool geometry

All diamond tools used in this research are manufactured such that the rake face is aligned with the (001) plane, and the flank face is tilted 6° from a (001) plane. Other tools may be manufactured with different clearance angles, and the rake face parallel to either the (001) or (011) plane. Also, many tools have a round cutting edge called a nose radius, which forms a nonplanar flank face. Different tool shapes and crystal orientations produce different lattice-dependant properties such as friction, wear and cleavage directions with respect to the sliding direction.

6.2 CRYSTAL ORIENTATION AFFECTS ON WEAR

Extensive research review and experiments conducted by Wilks and Wilks [3] found that the rate of wear on diamond depends on the sliding direction with respect to the crystal orientation of the abraded plane. Hitchner, Wilks and Wilks [25] found that volumetric removal rates of diamond can vary by an order of magnitude if the direction of sliding is changed by 45° when abrading with a cast-iron scaife or composite wheel with bonded diamond powder. Table 6-1 shows the relative rates of wear determined from Hitchner et. al. [25] for directions occurring on the rake face of tools used in this report. Values for rates of wear are useless to compare with diamond tool wear since Hitchner wore flat diamond diamond surfaces with a turning scaife or wheel; a method more attributable to grinding. However, the relative wear resistance should not be different.

Table 6-1: Comparison of wear when rubbing <100> and <110> directions on a (001) plane from [25]

	Nominal (001) Plane
<100>	More Wear
<110>	Less Wear

Wilks and Wilks [26] noticed in early experiments that rubbing in one direction can have different effects than rubbing in the reverse direction away. They determined that the

cause was due to misalignment of the sliding surface with the crystal plane it was supposedly aligned with. They found from goniometer measurements that the flat surfaces they were wearing were misaligned with the intended crystal plane by as much as 2° . Wilks and Wilks conducted many experiments abrading tilted diamond surfaces to examine these affects. They coined the terms “uphill” or “downhill” directions, as shown in the schematic in Figure 6-6. “Uphill” rubbing can be thought of as climbing the discontinuous crystal planes like stairs. Conversely, “downhill” rubbing is similar to descending these stairs.

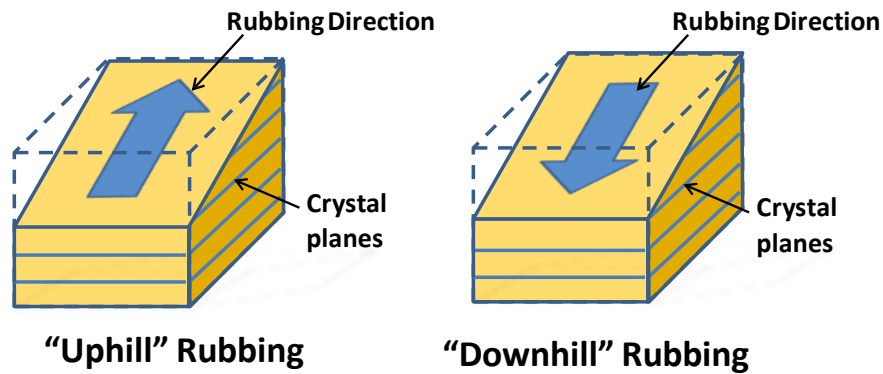


Figure 6-6: Schematic describing rubbing directions with respect to surfaces tilted about the true crystal planes.

In Wilks and Wilks’s experiments, a tilt of only 2° resulted in the depth of the wear scar for downhill abrasion double that for uphill abrasion. Table 6-2 summarizes their results abrading cubic (001) faces in two directions. As with Hitchner’s [25] experiments on rubbing directions, wear rate values cannot be directly compared to the cutting process, although relative rates may.

Table 6-2: Comparison of wear rates for a tilted (001) surface rubbing in the $\langle 100 \rangle$ and $\langle 110 \rangle$ directions from [26].

	Uphill	Downhill
$\langle 100 \rangle$	Less Wear	More Wear
$\langle 110 \rangle$	More Wear	Less Wear

Material flow on the rake face of diamond tools occurs in the $\langle 100 \rangle$ direction for tools with a carefully aligned (001) rake face. Material flow along the flank face occurs in a $\langle 100 \rangle$ downhill direction (see Figure 6-4 and Figure 6-5). From Table 6-1 and Table 6-2, the orientation of the tools used in the experiments conducted in this thesis are made such that the rubbing directions offer less resistance to wear when cutting.

Though the tools are manufactured for less wear resistance, this serves a functional purpose and is a widespread practice for manufacturing diamond tools. For tools used to create optical parts, the cutting edge must be as smooth as possible, since the shape of the edge is reproduced in the surface of the machined part. The tool flank face is less resistant to wear and easier to lap therefore tool requires less time to sharpen. The decrease in lapping time outweighs the costs attributed to tool wear [27]. Also, roughness of the diamond tool also changes with lapping direction. A worse surface finish is produced when lapping in a hard direction [3]. This worse surface finish results in a poorer quality cutting edge. Diamond tools intended to produce optical quality surface finishes require the smoothest edge possible, which can only be attained by lapping in soft directions on a single crystal tool, such as those used in this thesis.

While multiple tools with different crystallographic orientations may be difficult to manufacture, a change in the crystal reorientation can be accomplished with a simple experiment. All tools used in these experiments have a straight cutting edge, therefore they can be inverted so that the manufactured rake face becomes the flank face with no change to the intrinsic cutting geometry. Only the orientation of the crystallography is changed. Comparing tool wear from the inverted tool to the standard tool can determine whether the worn shape of the tool depends on cutting geometry or crystallographic orientation.

6.3 INVERTED TOOL EXPERIMENT

6.3.1 OBSERVED FACES AND NOMINAL FACES

Inverting the tool can create confusion when discussing certain parts of the tool. When inverted, the face of the tool that was intended to be used as the rake face by the tool manufacturer (nominal rake face) is no longer used for that purpose. Instead, the face that was intended to be the flank by the manufacturer (nominal flank face) becomes the “observed” rake face. In this report, “nominal” faces are those that are formed by the manufacturer to act as the rake or flank, regardless of how they are actually used in cutting. “Observed” faces are those that are used as the rank of flank, regardless of what they were intended to be used for by the manufacturer.

Figure 6-7 shows a schematic and photograph of the cutting process when the tool is used as intended by the manufacturer. A chip is formed along the tool rake face, therefore it is also the observed rake face. A person viewing this process would observe chip formation on the observed rake face, which happens to also be the nominal rake face.

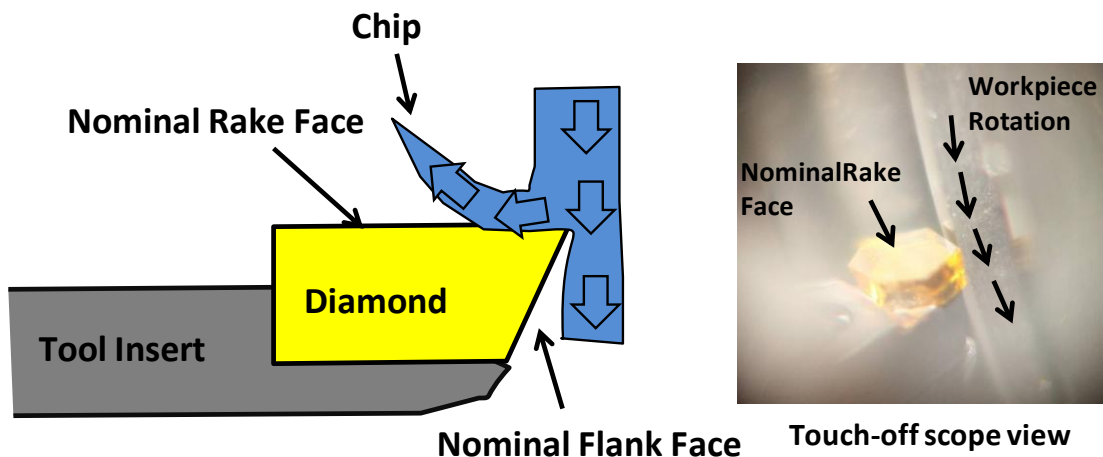


Figure 6-7: Schematic of tool orientation in standard cutting.

Figure 6-8 Figure 6-8 shows a schematic and photograph of the inverted cutting process. A person viewing this process would observe chip formation on the observed rake face,

although in inverted cutting this is the nominal flank face. Table 6-3 summarizes how nominal and observed rake and flank align in standard and inverted cutting.

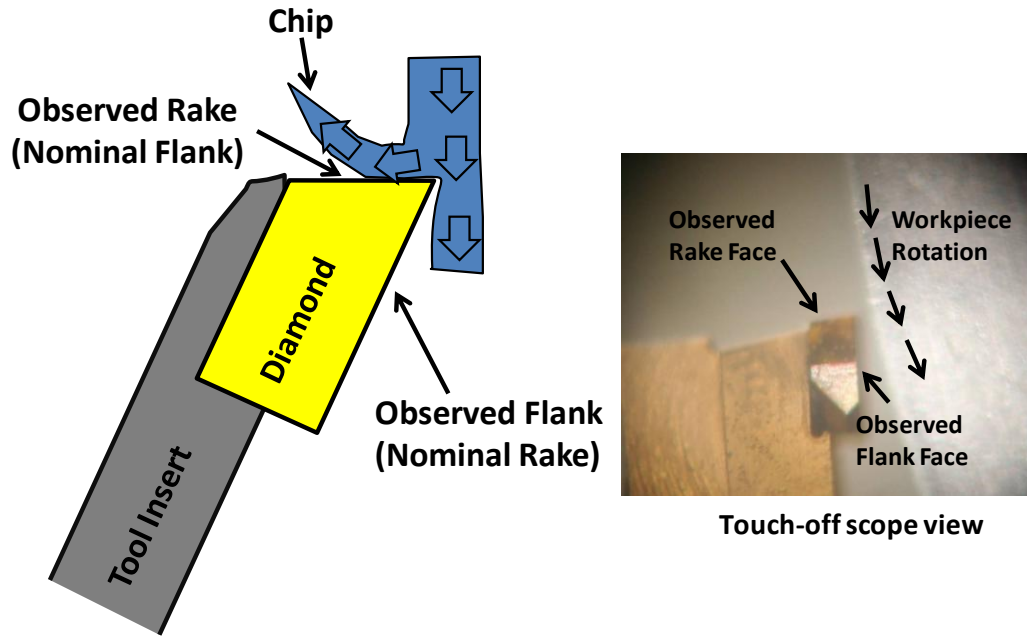


Figure 6-8: Schematic of tool orientation during inverted cutting.

Table 6-3: Comparison of rake and flank nomenclature for standard cutting and the inverted cutting experiment.

	Standard Cutting		Inverted Cutting	
	Nominal	Nominal	Nominal	Nominal
Observed Rake Face	Equal	Opposite	Opposite	Equal
Observed Flank Face	Opposite	Equal	Equal	Opposite

6.3.2 TOOL ORIENTATION AND CUTTING CONDITIONS

The tool needs to be accurately aligned to appear as in Figure 6-8, with the observed rake parallel to the diamond turning machine (DTM) stage. This was done by using a rotatable tool holder and aligning the tool using a straightedge protractor. Figure 6-9 shows this

process. For the observed rake face to be parallel to the DTM stage, the nominal rake face needed to be 84° from the stage (84° being the included angle of the tool). More accurate alignment of the observed rake face was accomplished by running a Federal indicator gauge along the diamond surface (moved along Z direction measuring Y displacement). Care was taken not to allow the gauge head to touch the cutting edge of the tool. The gauge was moved in the direction of the cutting edge, that is, it was moved along X direction but measuring the Y displacement. This aligns the cutting edge with the workpiece, so that the tool will contact the workpiece surface uniformly.

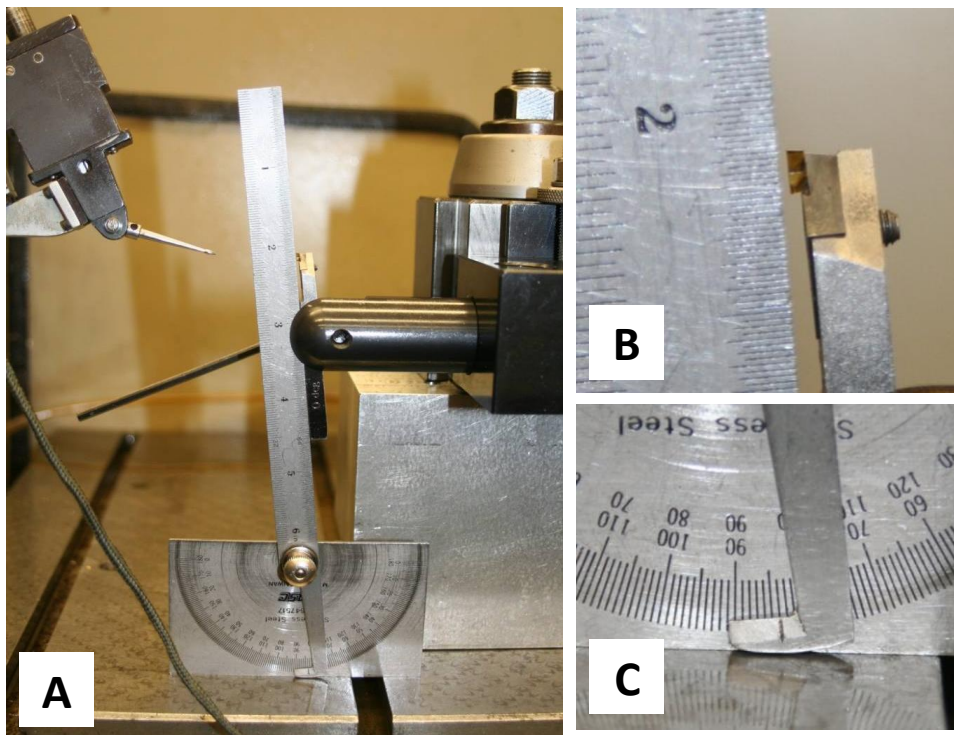


Figure 6-9: Straightedge protractor (A) used to roughly align the tool rake face (B) by 84° from the DTM stage (C)

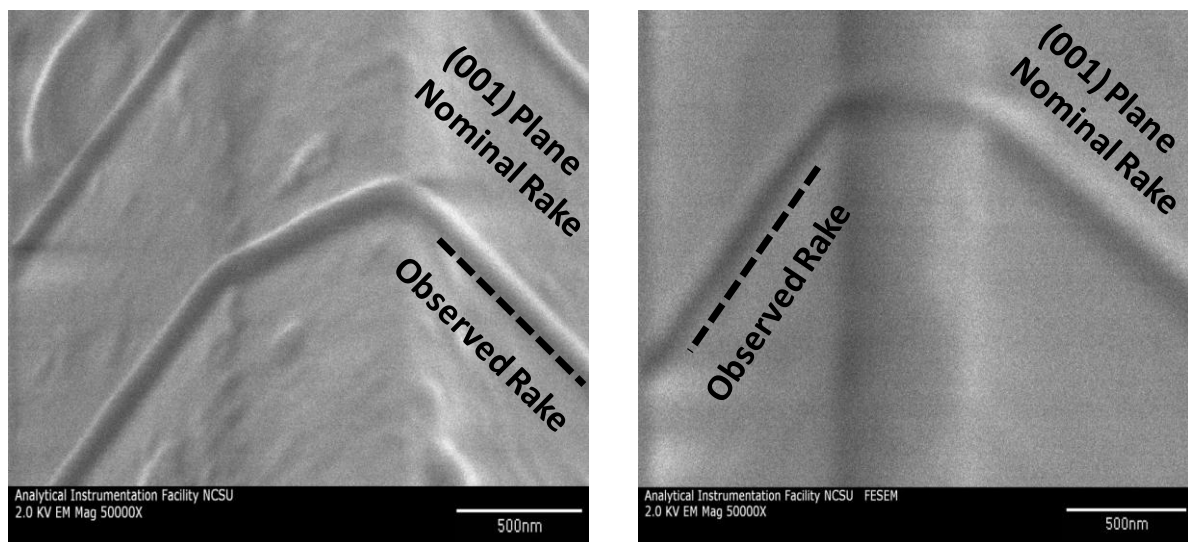
Lack of fine adjustment on the tool holder resulted in an observed rake angle of 0.7° instead of the desired 0° . Alignment in the direction of the cutting edge resulted in a tilt of 0.5° . This misalignment of the cutting edge requires that the tool be fed in $10\mu\text{m}$ before fully

coming into contact with the workpiece. These misalignments may cause variations in cutting conditions, although will unlikely have a great affect on the worn tool cross section.

Cutting conditions were the same as those conducted for the chemical wear experiments in Chapter 5. The same St1215 fins were machined, with a speed set at 2.12 m/s and depth of 1 μm . The fin was faced using a carbide tool to reduce runout and touchoff was accomplished using the machinist's microscope. A microstepping program was run at 200 nm steps until a chip could be seen. Force measurements were not taken since the rotating tool holder could not incorporate a load cell. EBID images of the worn to edge were taken after 5m of cutting.

6.3.3 WEAR RESULTS

Figure 6-10 compares unstretched EBID images of a diamond tool under standard cutting conditions and machining with the inverted tool. The nominal rake face, which is the (001) crystal plane, is in the same orientation in both images. The observed rake face, which coincides with the cutting direction, occurs on opposite sides of the cutting edge.



Standard Cutting

Inverted Cutting

Figure 6-10: Stretched EBID image of tool used in standard cutting St1215 (left) and inverted cutting (right) at 2.12 m/s and 1 μm DoC for 5m cut distance

Although wear rates cannot be accurately determined from the one wear measurement for the inverted tool, the shape of the EBID stripe lying across the cutting edge is markedly different. The EBID images for the standard and inverted tool were stretched according to the method outlined in Chapter 2.2.1, and traces of the EBID stripe were made that accurately portray the worn tool cross-section. Figure 6-11 shows these tool cross sections that were directly traced from the EBID images in Figure 6-10. Crystal orientation is the same in both images, while cutting direction and chip flow is different

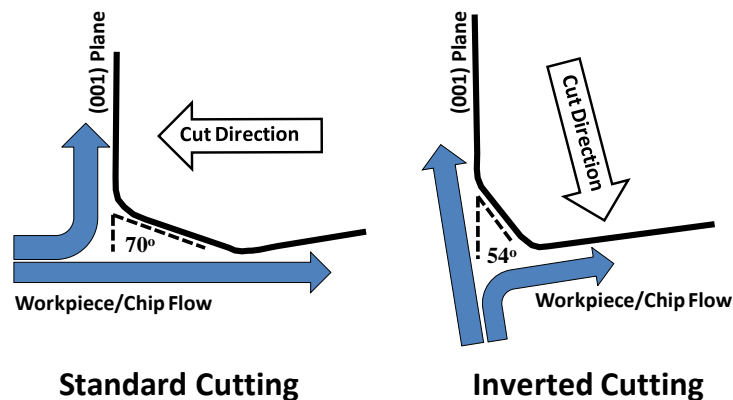


Figure 6-11: Worn tool cross sections traced from EBID images with crystal orientations aligned

The angle which the wear land occurs with respect to the (001) plane is different for both images. The angle was approximately 70° standard cutting tool and 54° for the inverted tool, a 16° difference. Since the crystal orientation is the same in both images, the difference in wear geometry stems from the different cutting direction and location of chip formation on the tool surface. This is easier to see when the worn tool cross section for the inverted tool is flipped and rotated so that the cut direction is the same in both images, as in Figure 6-12. Flipping the image so that the original ratio is unchanged does not change the relative geometry. The angle at which the wear land occurs with respect to the cut

direction is only 6° different for the inverted tool. The worn profile for the standard cutting tool (Figure 6-12, left) is the same as that in Figure 5-8.

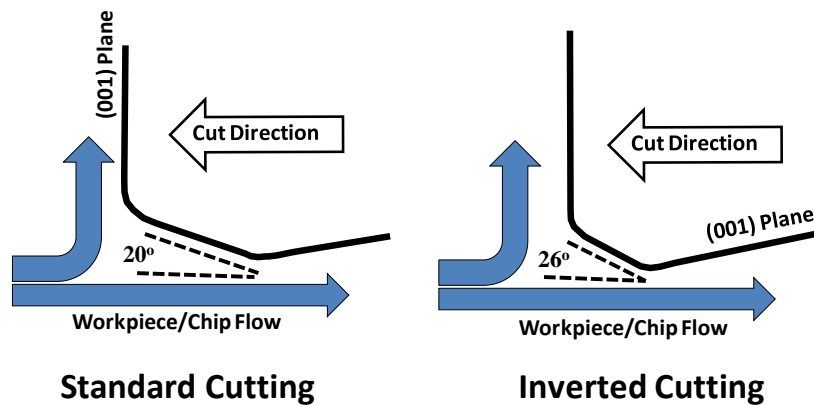


Figure 6-12: Worn tool cross sections traced from EBID images with cut directions aligned

6.4 CONCLUSIONS

The wear geometry of the inverted tool more closely resembles that of the standard cutting tool when comparing cut direction and chip formation locations and differs when comparing crystal orientation. This indicates that the effects of crystal orientation play less of a role in the worn tool geometry than does the cutting direction. Results from the inverted tool experiment, however, do not give any information on crystal orientation affects on wear rates. Also, since crystal orientation has less affect on wear geometry, it is unlikely that the wear land observed on the steel worn tool is due to crystallographic affects. In the formation of a chemical wear model, crystallographic affects can be neglected for a particular tool. Factors dependant on machining parameters, namely the tool temperature, should be taken into consideration.

7 CHEMICAL WEAR MODEL

Cutting temperatures depend on the cutting environment including thermal and mechanical properties of the tool, cutting fluid, and workpiece, along with cutting conditions such as speed, depth of cut and rake and tool geometry. It has been shown experimentally and analytically [28] that increasing the cutting speed results in an increase in tool temperature. Diamond machining experiments conducted by Casey and Wilks [29] on what is considered an abrasive material (LM13, an aluminum silicon alloy) found no change in the rate of wear when varying the cutting speed. The effect of temperature, therefore, can be studied experimentally by varying speeds, and any change in wear rate is indicative of a wearing process other than pure abrasion.

Most chemical reactions depend on the temperatures of the reactants. Diamond tool wear that is attributed to chemical processes is no different. Thornton and Wilks [8] found from static experiments that diamond graphitizes at lower temperatures in the presence of iron. They also noted that diamond does not wear in the presence of iron at room temperature and proposed that the high rates of wear they observed in cutting experiments were due to the clean surface interactions between the tool and workpiece. Noting wear from cutting steels is exacerbated by temperature, Brinksmeier and Glabe [30] attempted several methods to reduce process temperatures. Experiments in liquid nitrogen increased tool life (they defined when the tool edge recession equals depth of cut) by a factor of 10.

Paul and Evans et. al. [9] noted that the chemical reaction occurring in diamond tool wear on ferrous materials may be modeled using the Arrhenius equation, which relates the rate of volumetric changes in reactants with process temperature. Apart from studies of graphitization of diamond at temperatures above 2000K by Davies and Evans [31], no work was found that described the chemical wear of diamond tools with the Arrhenius equation.

Several authors have determined wear models for non-diamond machining that are related to the Arrhenius equation. Molinari and Nouari [32] modeled the crater wear of carbide

tools as a diffusive process, which combined analytical models for tool temperature profiles along the rake face with friction models and Ficks law of diffusion. Usui and Shirakashi [33] developed a wear model by combining abrasive and adhesive wear models. They determined the adhesive wear would depend on the temperature by an exponential function similar to the Arrhenius equation. They relied on analytical models for contact stress and chip velocity and experimentally determined tool temperature by implanting an insulated platinum wire within tool and connecting the free end to the workpiece. This formed a thermocouple junction between the platinum and workpiece and voltages relateable to temperature across the bimetallic junction were measured with a voltmeter.

The models by Molinari and Usui agreed fairly well with their respective experimental results but were only applied to the crater wear of tools not used in precision machining. From the EBID images taken of the steel worn tool (Chapter 3.2.3) one can note that the majority of wear of the diamond tool was due to the formation of a wear land rather than crater wear. Analytical models used by Usui and Molinari were derived assuming an unworn tool shape and would not likely work for diamond tools where the tool wear is on the same order of magnitude as the depth of cut. Experimental techniques are also made more difficult by the microscopic scale of diamond machining.

The complexities that occur in modeling the diamond turning process can be predicted using Finite Element Modelling (FEM). FEM allows the physical interactions in the cutting process to be modeled. Instead of simplifying the entire process to form general analytical models, FEM accounts for thousands of sub-processes and interactions with more robust analytical models. A commercially available finite element code called AdvantEdge by ThirdWave Systems was obtained to simulate the cutting process. AdvantEdge accounts for the interactions between the dynamic, mechanical, and thermal processes in metal cutting. Known worn tool shapes from EBID images can be input to the AdvantEdge model and the temperature distribution in the tool can be determined. These temperatures can then be

used in the formation of a model that describes the thermally activated chemical process of diamond tool wear.

7.1 THE ARRHENIUS EQUATION AND FICK'S LAW

Most literary references to chemical diamond tool wear attribute the volumetric loss of diamond to graphitization or diffusion into the contacting material (or workpiece in the case of diamond turning). Graphitization occurs when the atomic bonds at the surface of the diamond lattice break and form lower energy compounds (graphite). Diffusion occurs when separated carbon atoms enter as interstitials in the workpiece lattice. Chemical reactions such as graphitization follow the Arrhenius function, while diffusion processes follow Fick's Law. Both of these models are described by the same exponential function relating volumetric loss V to temperature T :

$$\dot{V} = \frac{d}{dt}V = A \exp\left[\frac{-E}{RT}\right] \quad (7.1)$$

In the Arrhenius function, the two experimentally determined constants E and A are the activation energy and the pre-exponential constant, respectively. The activation energy acts as a "barrier" to chemical reactions; with increasing thermal energy, a compound will transform into another lower energy compound once the energy surpasses the activation energy. The activation energy depends on the difference between the bond energies of the reacting solids and the transition complex and the pre-exponential factor A depends on the entropy [9] or the frequency of molecular collision occurring in the reaction. In Fick's law, the constant E and A are a similar energy barrier and entropy.

Determining the relative effects of graphitization vs. diffusion is difficult since both depend on the system temperature in the vicinity of the two interacting materials. For the predictive modeling of diamond tool wear, it is not necessary to discern these mechanisms, but make use of the fact that they are described by a single function. This function can describe the volumetric wear rate for a particular combination of workpiece and tool

materials. The activation energy and pre-exponential constant can be determined from a least squares linear fit to a log-log-plot of the volumetric wear rate vs. the inverse of the tool temperature:

$$\ln(\dot{V}) = \left(\frac{-E_a}{R} \right) \left(\frac{1}{T} \right) + \ln(A) \quad (7.2)$$

7.2 CUTTING TOOL TEMPERATURES

For the wear of cutting tools, volumetric wear loss can be determined by dividing worn volume of the tool by the cutting time. To model tool wear using the Arrhenius equations, however, the tool temperature needs to be known. Many analytical models have been developed to approximate cutting temperatures. Figure 7-1 shows a schematic of an orthogonal cutting heat transfer model. Most of the heat energy in the cutting process is generated in the primary deformation zone, and most heat is lost in the chip via mass transfer⁷. Abukhshim et. al. [28] noted that most analytical models differ in their estimation of energy partitioning. Different authors suggest different percentages of thermal energy flowing into the tool, chip, and workpiece, resulting in different estimates in tool surface temperature profiles and temperature gradients within the tool for the same input cutting conditions and materials. Though the energy partitioning has great affect on tool temperature results, it is difficult to predict without strong experimental verification.

⁷ Heat energy carried away from the primary shear zone with the chip is designated in [28] as being 'convection'. Convection is defined as a heat transfer process that is executed by the flow of a fluid [34]. In the case of metal cutting, heat energy contained within the chip 'flows' out of a control volume surrounding the heat generating processes. Since the chip is solid outside of the primary shear zone, this loss of heat energy is better defined as being due to mass transfer.

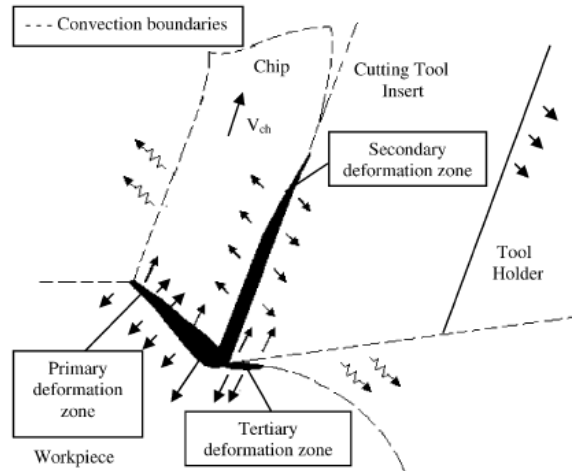


Figure 7-1: Schematic of heat transfer model in orthogonal cutting considering combined effects of three heat sources from Abukhshim et. al. [28].

Heat transfer in the metal cutting is not only challenging to model analytically, but the nature of the process makes validation through experimental results difficult as well. Several techniques are reviewed by [28]: the tool-work thermocouple technique uses the contact point of different tool and workpiece materials as a hot thermocouple junction. The tool-work thermocouple technique only gives an average temperature, however, and is subject to much noise. The embedded thermocouple technique relies on thermocouples planted in the tool or workpiece. This method was used by Usui and Shirakashi in [33]. This has limited response time, the embedded thermocouples reduce tool and/or workpiece strength, and the thermocouple introduces conductive properties into the system. Radiation techniques rely on infrared cameras and film to capture radiative heating. These are non-contacting measurement techniques, therefore temperatures aren't affected by the measurement setup. These techniques require line-of-sight measurement, and may be obstructed by chips. Also, relating infrared signal to temperature requires the emissivity of the surface to be known. Problems associated with these techniques are exacerbated in diamond turning due to sub-micrometer scale of the cutting process.

Ueda et. al [35] were able to measure the tool-chip contact temperature in DT by observing infrared radiation transmitted through the diamond tool to a fiber-optic cable, then measured in two infrared detectors with overlapping measurable ranges of infrared wavelength. Aluminum and copper were used as workpiece materials and machined at cut speeds of 8.6 m/s and 12.1 m/s, respectively. The specific alloy of the aluminum and copper and the depth of cut were not mentioned, however, though depth of cut was approximately 10 μ m based on a figure of the finite element model mesh. They noted that measured maximum temperatures on the rake face of the diamond tool increased rapidly to steady state and approached values of 190°C for aluminum and 220°C for copper.

The task of accurately modeling the heat transfer in the metal cutting is daunting due to the coupling of mechanical/material and heat transfer properties. In addition, cutting process temperatures depend on strain heating, frictional heating, conduction, mass transfer, convection, and to a lesser extent radiation. The only available method to model the cutting process and account for the effects is FEA.

7.3 FINITE ELEMENT ANALYSIS FOR TOOL TEMPERATURES

Several commercial finite element codes that model the cutting process are available. Three of which were reviewed and compared by Bil et. al. [36], including AdvantEdge by ThirdWave Systems, MSC.Marc, and Deform2D. They reported that despite differences in friction and rate-dependant material models utilized by the codes, resultant forces, temperatures, shear angles and chip thicknesses were within the same order of magnitude. One fault in all FE cutting codes, as noted by [36], is the lack of true experimental data for high strain rate (> 100 1/s) material sensitivity. Each of the three codes employs a different method to estimate or extrapolate higher rate conditions. Despite the differences, results from the three codes were not exorbitantly erroneous. Bil concluded that changing friction coefficients to match shear angle is the best way to tailor the simulation to fit experimental

data, though no code was able to concurrently predict forces, chip thicknesses, and temperatures all to within 50% of experimental data.

Despite the inaccuracies in modeling all aspects of machining, the lack in ability to measure tool temperatures experimentally promotes FE cutting models for temperature prediction. A copy of AdvantEdge was procured along with an academic license. A 2D orthogonal machining model was created AdvantEdge and friction and hardness properties were varied in the software to match experimental chip thicknesses and cutting forces. Once suitable values for friction and hardness were found, tool temperatures required for the Arrhenius equation wear model were extracted.

7.3.1 ADVANTEDGE FINITE ELEMENT MODELLING

In the 2-D turning modes in AdvantEdge, the workpiece and tool are meshed using 6-noded triangular elements. This element type is set by the software and cannot be changed. Two domains are modeled: one for the stationary tool and one for the advancing workpiece. The tool domain has a set mesh that doesn't change, while the workpiece mesh is constantly regenerated with each iterated time-step. AdvantEdge accounts for the coupling of thermal and mechanical properties by utilizing separate meshes for thermal and mechanical calculations [37]. Elements in a Lagrangian FE model of cutting will eventually deform to a point that will render the system unsolvable. AdvantEdge utilizes a mesh regenerating algorithm that forms new elements in place of those that have deformed beyond a certain criteria. Implicit time integration scheme is used, despite a required maximum timestep for stability [37].

Heat energy is generated by either plastic work or frictional heating in Third Wave. The specific thermal energy created by plastic work is determined by multiplying the specific plastic work (stress times strain rate divided by density) by a constant fraction. The specific thermal energy due to frictional heating is determined by the dot product of the surface traction vector with the relative velocity between the tool and workpiece. The total specific

friction energy is then divided between the tool and workpiece based on their respective densities, thermal capacities, and conductivities via the following:

$$\frac{h_1}{h_2} = \frac{\sqrt{k_1 \rho_1 c_1}}{\sqrt{k_2 \rho_2 c_2}} \quad (7.3)$$

Heat energy generated within the primary shear zone and frictional contact is transferred to tool via conduction and loss through isothermal boundaries on the opposite side of the tool.

7.3.2 ST1215 ADVANTEDGE CUTTING MODEL

Advant Edge supplies a micro-scale orthogonal cutting mode appropriate for diamond turning simulations. Simulations were created in this mode that mimic the cutting conditions used for the St1215 wear experiments. AdvantEdge allows the user to input custom thermal material properties for the tool but also has a library of material models including diamond. The material properties of the library tool materials are proprietary, and are not supplied by ThirdWave Systems. Table 7-1 gives properties assumed to be used by AdvantEdge for diamond.

Table 7-1: Material and thermal properties of diamond.

Material	Diamond^a
Density	3.2 g/cc
Yield Strength	415 MPa
Vickers Hardness	167 Bhn
Thermal Conductivity	2000 W/m-K

a – Values determined from [15]

The thermal conductivity of diamond is 5X that of copper, which is considered highly thermally conductive. The specific thermal capacity of diamond varies greatly around temperature near 300 K. Victor [38] determined the heat capacity in gem quality natural

diamonds and found approximate values of 0.5 J/g-K to 1.3 J/g-K over the range of 300K to 600K.

AdvantEdge also supplies a material library of various workpiece materials. The library doesn't contain AISI 1215 which was used in the wear experiments. A user defined material model can be made, but complex material properties used by AdvantEdge's thermal softening, strain hardening, and strain-rate models could not be found for AISI 1215 steel. AISI 1118 steel was available in the AdvantEdge library, and has similar properties to AISI1215. Table 7-2 compares material property values for these materials. AISI 1118 was used in the AdvantEdge simulations in lieu of AISI 1215 steel.

Table 7-2: Comparison of material properties for 1215 Steel (used in experiments) and 1118 steel (available in AdvantEdge material library)

Material	AISI 1215 Steel^a	AISI 1118 Steel^{a,b}
Density	7.87 g/cc	7.87 g/cc ^a
Yield Strength	415 MPa	315 MPa ^b
Hardness	167 Bhn	150 Bhn ^b
Thermal Conductivity	51.9 W/m-K	49.8 W/m-K ^b

a – Values determined from [15]

b – Values determined from ThirdWave AdvantEdge material database

AdvantEdge does not account for temperature dependant thermal capacities of diamond, but at temperatures of 300K the heat partitioning used by AdvantEdge in Equation (7.3) gives a diamond to steel ratio of 4:1. This means about 19.6% of frictional heat goes into the steel workpiece and about 80.4% into the diamond.

Thermal boundaries used in the AdvantEdge simulations are shown in Figure 7-2. These boundary conditions are set by AdvantEdge for the standard workpiece used in the model.

AdvantEdge also applies these same conditions to standard tools, therefore they were applied to the custom tool designed for this simulation.

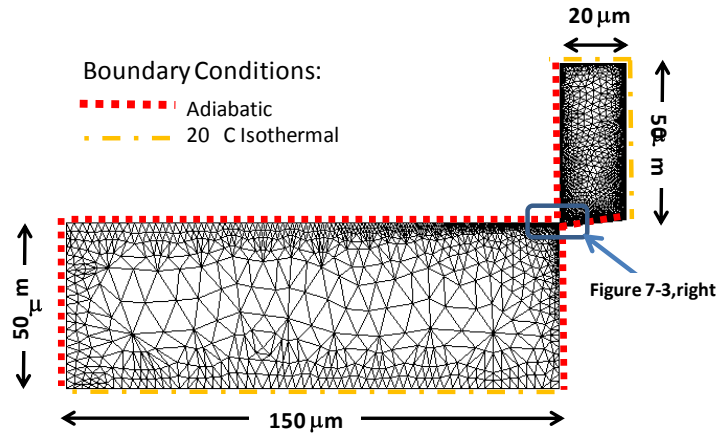


Figure 7-2: Mesh and boundary conditions for the AdvantEdge cutting model

Much of the cutting process is affected by the tool edge. To better replicate experimental values, a custom tool was created in AdvantEdge that is the same as the tool edges measured experimentally via EBID. Figure 7-3 shows an example of an EBID image used to determine the dimensions of a custom FEM tool shape.

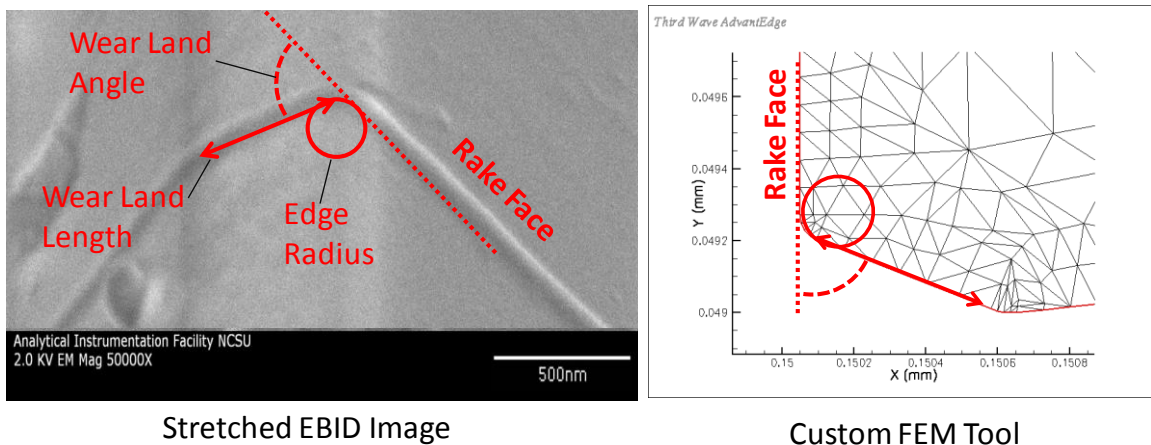


Figure 7-3: (Left) Stretched EBID image of diamond tool worn after 10 m distance at 2 m/s and 1 μm depth of cut. (Right) Tool dimensions are replicated in FEM model.

7.3.3 FEM MODEL VALIDATION

Bil. et. al. [36] noted that the friction coefficient should be changed to match FEM cutting simulation results to experimental results. In AdvantEdge FE, the same friction coefficient is used on all surfaces of the tool. Friction was varied for a 2D AdvantEdge cutting simulation utilizing the same machining conditions and custom tool edge shown in Figure 7-3. Figure 7-4 shows average force results from 4 simulations that varied friction parameter. A friction parameter of 0.8 resulted in simulated average tool forces within 5% of those measured experimentally cutting St1215.

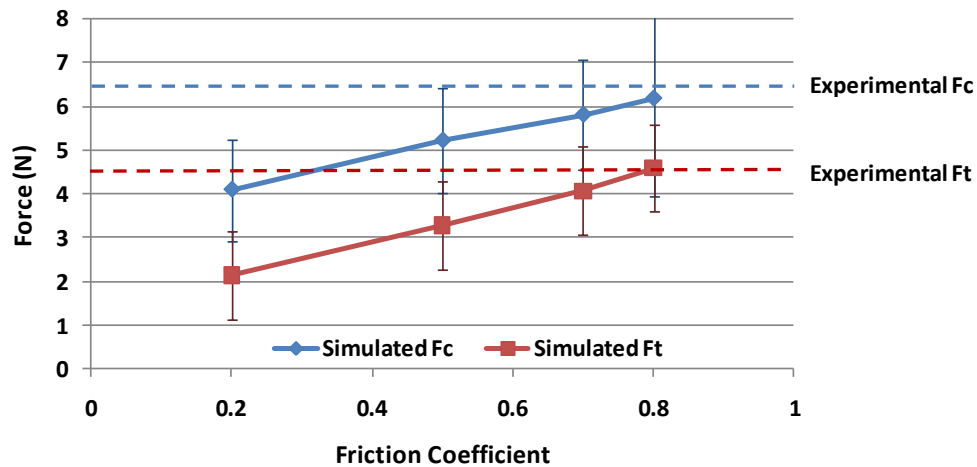


Figure 7-4: Affects of varying friction coefficient in AdvantEdge FE 1118 steel model. Error bars show one standard deviation.

The ratio of cutting forces to thrust forces is important as well as their individual magnitude. Increased wear of a tool causes thrust forces to increase at a higher rate than cutting forces [5,6,20,21], which gives a particular force ratio for a state of wear when diamond machining a certain material. The force ratios for the 4 simulations are compared to the experimental value in Figure 7-5. A coefficient friction of 0.7 gave a simulated force ratio value with only 1.1% error.

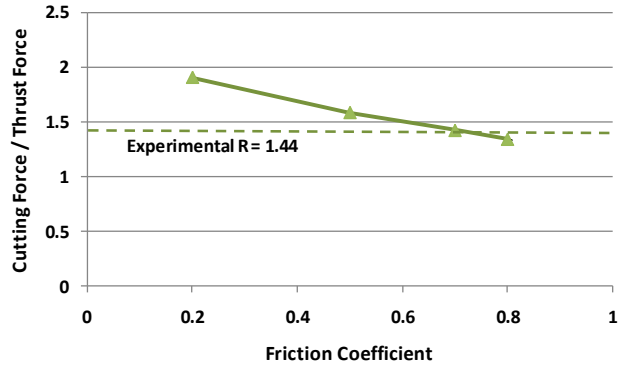


Figure 7-5: Change in ratio of cutting force to thrust force with friction coefficient for 4 AdvantEdge cutting simulations of St1118.

Increasing the friction coefficient also changes the chip thickness and shear angle of the simulations. Figure 7-6 shows the chip formation while simulating cutting with 4 different friction coefficients. Chip thickness increased with increased friction causing the shear angle to decrease. Black arrows in Figure 7-6 show locations where chip thickness is measured.

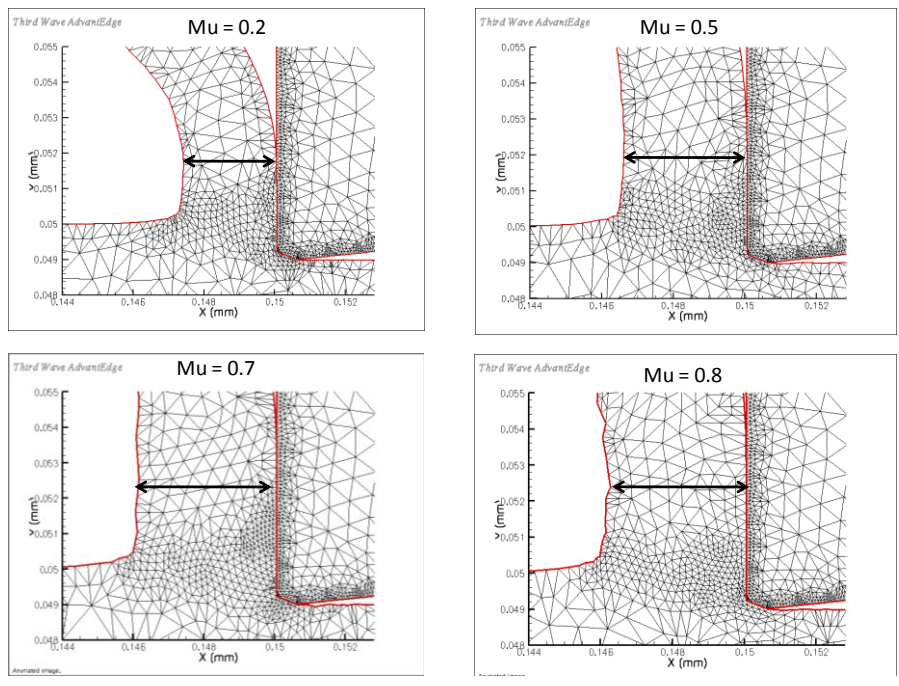


Figure 7-6: Chip sizes for 4 values of friction coefficient in AdvantEdge St1118 simulation.

Chips were collected after machining St1215 at 2 m/s and 1 μm depth of cut. Chip thickness was measured in an SEM by focusing on the edge of the chip and using the SEM image analysis tools to measure chip thickness, shown in Figure 7-7. The chip thickness varied over the length of the chip, though it remained within 0.5-1 μm thick.

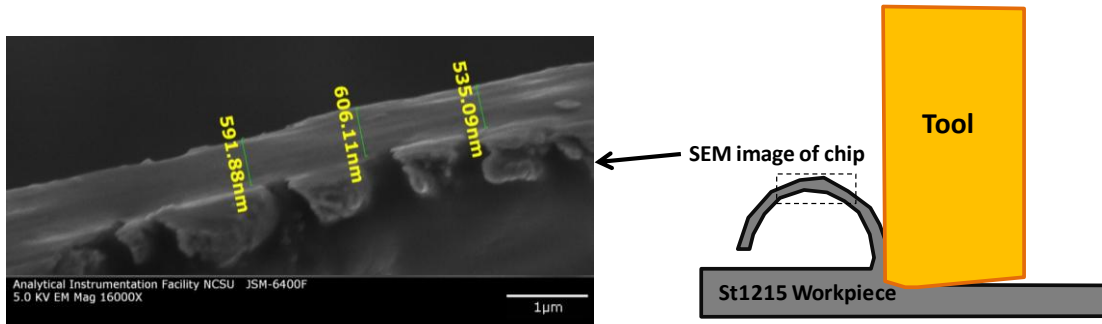


Figure 7-7: SEM image of chip edge collected after machining St1215 at 2 m/s and 1 μm depth of cut.

Chip thicknesses from simulations in Figure 7-7 were compared chips collected from machining experiments shown in Figure 7-7. Chip thicknesses simulated in AdvantEdge overestimated those collected experimentally by at least 200%, as shown in Figure 7-8. Shear angles in the primary deformation zone can be estimated by the ratio of depth of cut to chip thickness.

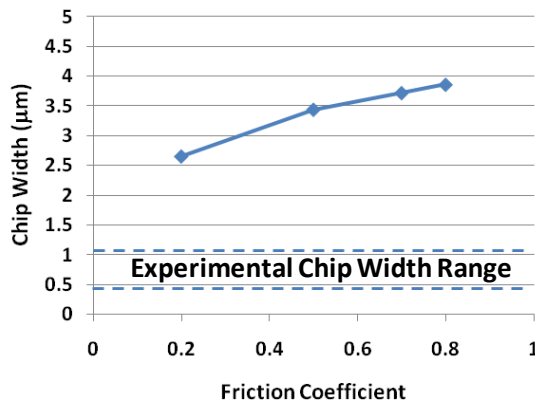


Figure 7-8: AdvantEdge simulated chip width compared to those measured experimentally.

The disagreement between simulated chip thickness and experimental chip thickness show that the friction coefficient cannot be adjusted to match shear angle, in accordance with the suggestion by Bil [36]. Simulated values of chip width shown in Figure 7-8 show that this is not practical in AdvantEdge and erroneous chip thickness is unavoidable for these simulations.

Acquiring tool temperature data is the goal of these FE cutting simulations. Maximum tool temperature was determined for the 4 simulations varying friction. Figure 7-9 shows these temperatures, which only varied 6° C over the range of $\mu = 0.2..0.8$.

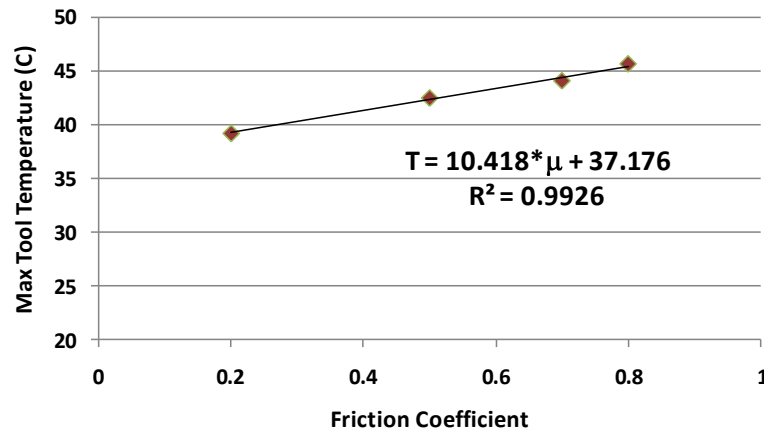


Figure 7-9: Maximum tool temperature determined from AdvantEdge simulations cutting St1118 for varying friction coefficient. Standard deviation of data noise is $< 0.25^{\circ}\text{C}$.

Tool forces could be accurately predicted by the AdvantEdge simulations if friction is set to 0.7-0.8. Chip thickness and shear angle, however, could not be accurately predicted by the FE model for any value of friction. Simulated tool temperatures only increased 10% when friction was increased 300%. Friction values for further simulations were set to the default value of 0.3. Despite erroneous tool forces and chip thickness at this value, simulated tool temperatures are not greatly affected, therefore the default value for friction of 0.5 is assumed. Simulations utilizing the custom tool shape in Figure 7-3 and St1118 as workpiece material were created for the machining speeds used in experiments in chapter 5.

Results from several more simulation demonstrate trends in tool forces, tool temperature and chip temperature at different cutting speeds. The relationship between cutting speed and tool temperature are predicted by the FEM model, shown in Figure 7-10.

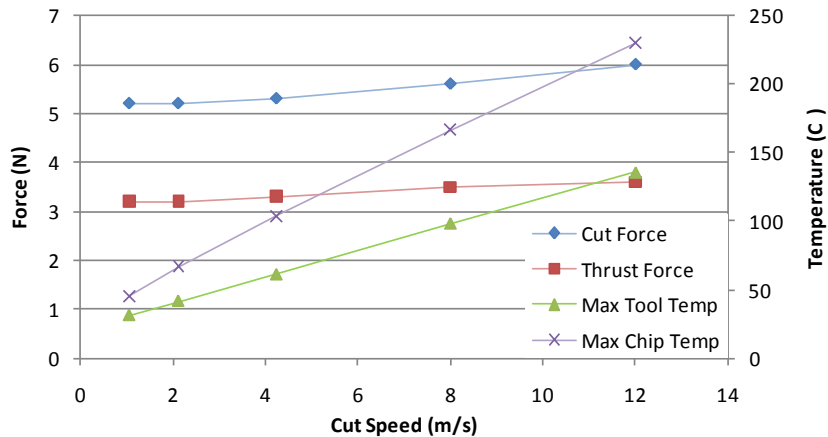


Figure 7-10: AdvantEdge simulation as a function of cutting speed for 1118 steel at 1µm DoC.

Ueda et. al. [35] measured maximum tool temperatures cutting aluminum and copper with a diamond tool by measuring infrared signals through the diamond (see Section 7.2). They measured maximum tool temperatures of 190°C for aluminum at 8.6 m/s machine speed, and 220°C for aluminum at 12.1 m/s machine speed. Though conductivities and thermal diffusivities of these materials are different than the St1118 simulations of Figure 7-10, their conductivities are all less the 10% than that of diamond. Frictional energy partitioning governed by equation 7.3 will be similar for aluminum, copper, and steel. Therefore, it is reasonable to assume the simulated tool temperatures given in Figure 7-10 are accurate at to at least an order of magnitude due to similar experimental temperatures from [35]. However, lack in ability to experimentally verify temperature results from FE simulations leads these temperatures to be subject to high error, yet these are the only available measure of diamond tool temperature. Further AdvantEdge cutting simulations of copper

and aluminum to compare with [35] may explain more about temperature prediction capabilities of the FE code, particularly in micron-scale cutting with diamond tools.

7.4 RESULTS

7.4.1 ADVANTEDGE SIMULATION RESULTS

Contour plots of temperature from the AdvantEdge models showed higher temperatures in the primary and secondary zones depicted in Figure 7-1. Figure 7-11 shows temperature contours for the 1.06 m/s and 4.24 m/s simulations. Temperatures within the chip and tool were higher at the higher cutting speed as expected.

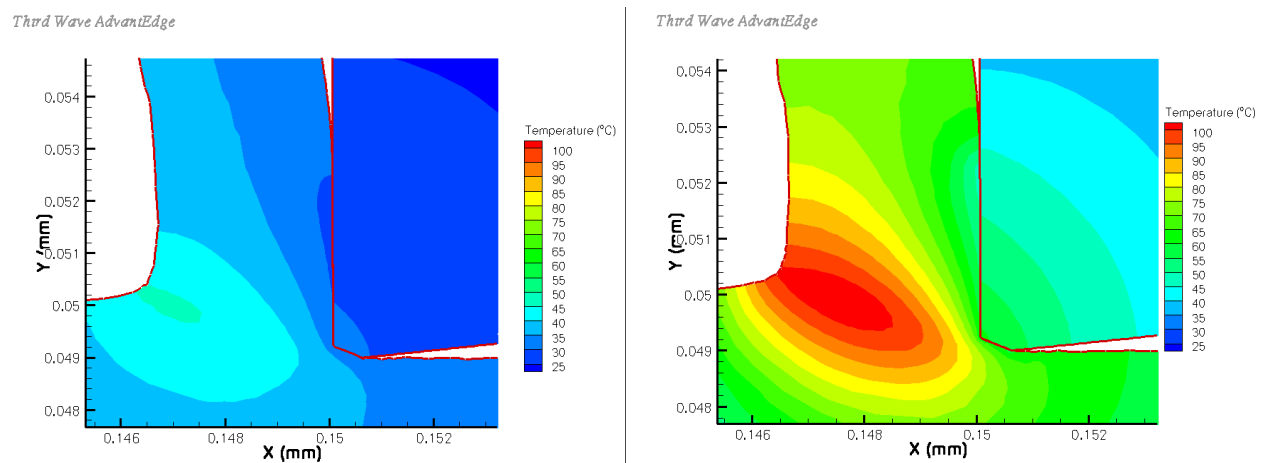


Figure 7-11: Steady state temperature contour plot of 1.06 m/s (left) and 4.24 m/s (right) simulations.

Measured tool forces and maximum tool temperature are plotted in Figure 7-12. AdvantEdge provides a force and temperature data filter which uses a 10th order polynomial best fit curve to trace the data. Noise in the force data had a standard deviation of 1.2 N and noise in the temperature data had a standard deviation of 0.2 °C. Many factors contribute to this noise including time-step size used in the numerical integration, simulated vibration intrinsic to the frictional contact algorithm, and overall discretization of the system. As with cutting experiments, the steady state tool forces changed little with

increase in cut speed. The force magnitudes, however, were less than those measured experimentally (Chapter 5.2.1). Measured forces were approximately 4.5 N and 6.5 N for thrust and cut force, respectively, while AdvantEdge results gave thrust and cut forces at 3.2 N and 5.2 N. Material properties cannot be changed for materials supplied in the AdvantEdge library, but tool friction parameters could be changed to match FEM forces with experimental forces.

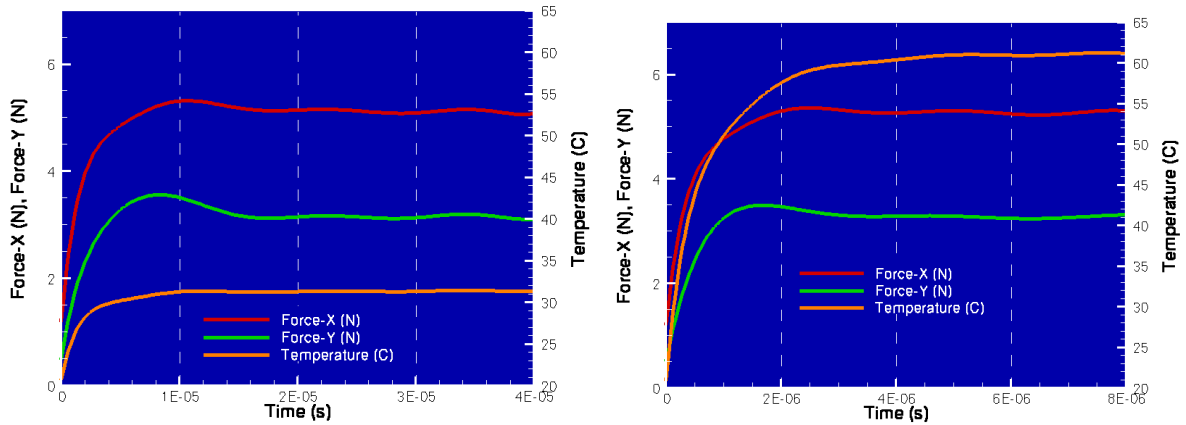


Figure 7-12: Predicted cutting forces and maximum tool temperatures for 1.06 m/s (left) and 4.24 m/s (right)

Temperatures of 62°C at 4.24 m/s and 40°C at 1.06 m/s were found from data shown in Figure 7-12. Figure 7-13 shows a log-log plot of this data. Tool wear volume rates determined via SWLI wear land measurements can be used with temperatures determined from AdvantEdge to find the Arrhenius constants.

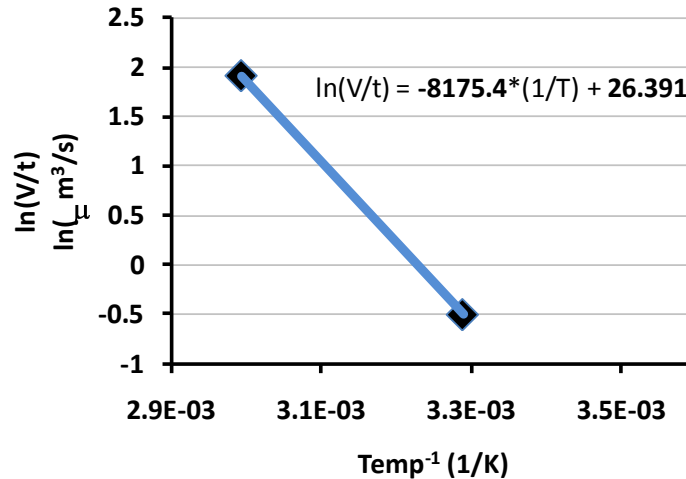


Figure 7-13: Arrhenius plot of diamond tool wear on low carbon steel

From the equation of the line determined in Figure 7-13, Arrhenius constants can be determined using Equation (7.2). Using a value of 8.3144 J/K-mol for the universal gas constant, the pre-exponential constant A is determined to be $2.894 \cdot 10^{11} \mu\text{m}^3$, and the activation energy E_a as 67.973 kJ/mol.

7.5 DISCUSSION

Material properties of AISI 1118 steel used in the simulations and AISI1215 steel used in experiments were assumed to be similar (Table 7-2) but many properties used in the FE simulations were not known. Strain-hardening and thermal-softening properties cannot be determined from the AdvantEdge material library nor be found in literature. Large differences in these properties for 1118 steel and 1215 steel would give rise simulation results that do not properly model experimental conditions. However, similarities in hardness, yield strength, elastic modulus, conductivity, etc. would mean that more complicated properties are likely similar as well.

Results from initial AdvantEdge cutting simulations were compared with experimentally measured tool forces and chip thicknesses. Varying the coefficient of friction allowed tool forces to be accurately predicted, but chip thickness was inaccurately modeled for all values

of friction. Tool temperatures were the desired results from the FE models, but varied little with increase in friction, therefore the default friction coefficient of 0.5 was assumed. Comparison of FE results to experimental results from [35] showed predicted temperatures are reasonable, but unverifiable. Data determined from 2.12 m/s experiments couldn't be used to determine the Arrhenius equation constants and provide a third data point in Figure 7-13. Tool wear measurements were only taken using the EBID method, while the 1.06 m/s and 4.24 m/s cut experiments combined EBID with SWLI wear land measurements to determine worn volume. Also, the 2.12 m/s experiment was conducted as an initial experiment to observe what wear would occur, and not continued past 20 m. Another cut experiment should be conducted at 2.12 m/s with cut distances up to 100 m using the same SWLI wear land techniques as used in the slow and high speed experiments.

The activation energy of 67.973 kJ/mol is far less than that observed by [31]. Activation energies of approximately 730 ± 50 kJ/mol were measured by heating diamond in vacuum up to 2000 °C, removing the graphitized surface with acid, then comparing the weight of the remaining pure diamond⁸. Thornton and Wilks [4] noted that the clean contact between the diamond and steel workpiece would likely require lower temperatures to initiate graphitization and proposed using the cutting process as a means to study clean surface interactions since perfectly surfaces untouched by the atmosphere are difficult to attain by any other means. The low activation energy observed is likely a result of the clean surface interaction coupled with catalytic affects of the steel.

⁸ They related the Arrhenius equation to the etch rate, measured in length per time, instead of volumetric rate. If the etched surface maintains a constant surface area, both methods will result in the same activation energy. A constant surface area can be assumed if the ratio of surface area to etch depth is very large, which is usually the case.

8 CONCLUSION

Though there is much information regarding the tribological properties of diamond [3], few have observed and measured tool wear after diamond machining [4-6,10-14]. Even fewer studies have directly related experimental results to wear models that can be compared to more well known wearing mechanisms. A direct reason for this lack in scientific background is the inherent difficulty measuring the microscopic wear of diamond tools. This thesis provides improved methods of diamond tool wear measurement, demonstrates two hypothesized wearing mechanisms and provides the formulation of models that can be used to compare diamond tool wear among multiple workpiece materials.

Methods for analyzing tool wear were developed in Chapter 2. Improved techniques were developed for a previously designed tool measurement method called EBID [4,13]. This includes a Matlab script for calculating wear geometry from EBID images and a method using a scanning white light interferometer to make more rapid wear measurements. The Matlab script reduces subjectivity errors introduced when analyzing EBID images and incorporates a tool to calculate cross-sectional worn area. The SWLI wear measurement method allows a user to make tool wear measurements more rapidly than the EBID method without incurring significant error.

Wear experiments on Al6061 and analysis of results were conducted in Chapters 3 and 4. The EBID method was used to observe and measure trends in wear geometry with progressive machining. Observation of the wear geometry was used to formulate a simple tool force model that was used to extract a normal force from measured tool forces. This normal force, in conjunction with machining distance, was used to compare the wear of a diamond tool machining Al6061 with other materials via Archard's wear law [2]. An Archard wear constant of $0.057 \mu\text{m}^3\text{N}^{-1}\text{m}^{-1}$ with 97% correlation was determined, which demonstrates that diamond tool wear on Al6061 is an abrasive process. This wear constant is much lower than metal-on-metal wearing contacts [22], which demonstrates the

relatively high abrasive wear resistance of diamond. The method provided here is a simple means to compare abrasive diamond tool wear among different workpiece materials, which may lead to more educated decisions in choosing materials to for diamond turning.

Wear experiments on St1215 were conducted in Chapters 5 and 6. High wear rates on diamond machining steel were reported in literature and a chemical interaction between the diamond and ferrous alloys was suggested as a reason [1,7-9]. It was hypothesized that chemical wear of diamond tools could be modeled using the Arrhenius equation.

Tool wear measured via EBID and SWLI methods after diamond machining steel showed comparable wear to that from Al6061 but at machining distances 1000x less. Wear geometry was observed on the St1215 tool that was different than the Al6061 tool. It was hypothesized that different crystallographic planes on the rake and flank face of the tool would introduce different wear rates causing the observed geometry. An experiment was conducted in Chapter 6 in which the tool was reversed such that the manufactured rake face acted as the flank. This essentially changed the crystal orientation without changing the shape of the tool with respect to the workpiece. Wear measurements on the inverted tool showed that the wear pattern observed after machining St1215 depended on the orientation of the tool with respect to the workpiece and not the orientation of the crystal lattice.

To attribute the tool wear from steel to a chemical process, tool temperatures needed to be determined. A commercial finite element code called AdvantEdge by ThirdWave Systems simulates the cutting process and is capable of modeling tool temperatures. Verification studies were performed that varied the tool friction coefficient to match simulated tool forces and chip thickness to experimental results [36]. The simulation was capable of accurately predicting tool forces though simulated chip thicknesses were at least 200% larger than chips collected after machining experiments. Though friction was varied by 300%, tool temperatures varied less than 10%. Since tool temperatures were desired yet varied little with friction, the friction coefficient was left at the default setting of 0.5.

Simulated tool temperatures were combined with tool wear measurements from EBID and SWLI methods to determine coefficients of the Arrhenius equation. A pre-exponential constant of $2.894 \cdot 10^{11}$ and activation energy of 67.973 kJ/mol were determined for the diamond machining of St1215. This activation energy is low compared to that determined for the graphitization of diamond in vacuum [31]. This adds to predictions [9] that steel works as a catalyst as the diamond is converted to graphite or lower energy molecular forms, resulting in the loss of volume of the diamond tool.

9 REFERENCES

1. Crompton, D., Hirst, W., Howse, M.G.W., The wear of diamond, Proc. R. Soc. London Ser. A 333 (1973) p.435-454
2. Archard, J.F., Contact and rubbing of flat surfaces, J. Appl. Phys. 24 (1953) 981
3. Wilks, J., Wilks, E., *Properties and Applications of Diamond*, Butterworth-Heinmen Ltd., Oxford, 1991
4. Drescher, J., Scanning electron microscopic technique for imaging a diamond tool edge, *Precis. Engr.* 15 (1993) 112-114.
5. Drescher, J.D., *Tool Force, Tool Edge, and Surface Finish Relationships in Diamond Turning*. PhD. Dissertation, North Carolina State University (1991)
6. Arcona, C., Dow, T.A., An empirical tool force model for precision machining, *J. Manuf. Sci. Eng.* 120 (1998) 700-708
7. Thornton, A.G., Wilks, J., Clean surface reactions between diamond and steel, *Nature* 274 (1978) 792-793
8. Thornton, A.G., Wilks, J., The wear of diamond tools turning mild steel, *Wear* 65 (1980) 67-74
9. Paul, E., Evans, C.J., Mangamelli, A., McGlaufflin, M.L., Povlani, R.S., Chemical aspects of tool wear in single point diamond turning, *Precis. Engr.* 18 (1996) 4-19
10. Asai, S., Taguchi, Y., Horio, K., Kasai, T., Kobayashi, A., Measuring the very small cutting-edge radius for a diamond tool using a new kind of SEM having two detectors, *CIRP Ann-Manuf. Tech.* 39 (1990) 85-88.
11. Li, X.P., Rahman, M., Liu, K., Neo, K.S., Chan, C.C., Nano-precision measurement of diamond tool edge radius for wafer fabrication, *J. Mat. Proc. Tech.* 140 (2003) 358-362.
12. Gao, W., Motoki, T., Kiyono, S., Nanometer edge profile measurement of diamond cutting tools by atomic force microscope with optical alignment sensor, *Prec. Eng.* 30 (2006) 396-405
13. Shi, M., Scattergood, R., Dow, T.A., Diamond tool wear measurement by EBID, 2009 ASPE Annual Conference (Pending Publishing)

14. Arcona, C., Tool force, chip formation, and surface finish in diamond turning, PhD. Dissertation, North Carolina State University, 1996
15. Matweb.com Material Property Data <www.matweb.com> [accessed 10 December 2009]
16. Tylczak, J.H., Abrasive Wear. in: P.J. Blau et al. ASM Handbook, Vol. 18, Friction, Lubrication and Wear Technology, ASM International, USA pp.184–190, 1992
17. Merchant, M.E., *Mechanics of the Metal Cutting Process*, J. Appl. Phys. 16 (1945) 267D.
18. Shaw, M.C., *Metal Cutting Principles*, Oxford University Press, New York, 1986
19. Kovrizhnykh, A.M., trans. Gorin, S., Generalization of the Lee–Shaffer solution in the theory of metal cutting, Doklady Phys. 53 (2008) 11-14
20. Smithey, D.W., Kapoor, D.W., DeVor, R.E., A new mechanistic model for predicting worn tool cutting forces, Mach. Sci. and Tech. 5 (2001) 23-42
21. Waldorf, D.J., DeVor, R.E., Kapoor, S.G., An evaluation of ploughing models for orthogonal machining, J. Manuf. Sci. Eng. (1999) 550-558
22. Archard, J.F., Hurst, W., The wear of metals under unlubricated conditions, Proc. R. Soc. London, Ser. A 236 (1956) 397-410
23. Shi, M., Thermochemical Tool Wear in Orthogonal Diamond Cutting Steel and Stainless Steel, M.S. Thesis, North Carolina State University, 2010
24. Schneider, G., *Cutting Tool Applications*, GMRS Assoc., Detroit, 2002
25. Hitchner, M.P., Wilks, E.M., Wilks, J., Polishing of diamond and diamond composite materials, Wear 94 (1984) 103-120
26. Wilks E.M., Wilks, J., The resistance of diamond to abrasion, J. of Phys. D, 5 (1972) 1902-1919
27. Hunter, M., <mhunter@chardontool.com> (2009, December 30) [Personal email]
28. Abukhshim, N.A., Mativenga, P.T., Sheikh, M.A., Heat generation and temperature prediction in metal cutting: A review and implications for high speed machining, Int. J. of Mach. Tools and Manuf. 46 (2005) 782-800

29. Casey, M., Wilks, J., Some experiments to study turning tools using the scanning electron microscope, *Int. J. of Mach. Tool Design and Re.*, 16 (1976) 13-22
30. Brinksmeier, E., Glabe, R., Advances in the precision machining of steel, *CIRP Ann-Manuf. Tech.* 50 (2001) 385-388
31. Davies, G., Evans, T., Graphitization of diamond at zero pressure and at high pressure, *Proc. R. Soc. London. Ser. A* 328 (1972) 413-438
32. Molinari, A., Nouari, M., Modeling of tool wear by diffusion in metal cutting, *Wear* 252 (2002)135-149
33. Usui,E., Shirakashi, T., Analytical prediction of cutting tool wear, *Wear* 100 (1984) 129-151
34. Bejan, A., *Heat Transfer*. New York: John Wiley and Sons, Inc., 1993.
35. Ueda, T., Sato, M., Nakayama, K., Temperature of a single crystal diamond tool in turning, *Annals of the CIRP* 47 (1998) 41-44
36. Bil, H., Kilic, S.E., Tekkaya, A.E., A comparison of orthogonal cutting data from experiments with three different finite element models, *Int. J. Mach. Tools Manuf.* 44 (2004) 933-944
37. Marusich, T.D., Ortiz, M., Modelling and simulation of high speed machining, *Int. J. Num. Meth. in Engr.* 38 (2005) 3675-3694
38. Victor, A.C., Heat capacity of diamond at high temperatures, *J. of Chem. Phys.* 36 (1962) 1903-1911

10 APPENDICES

10.1 TOOL FORCE AND WEAR DATA FOR EXPERIMENTS ON AL6061

Table 10-1: Force data for multiple depth of cut machining Al6061

DoC	Plunge		Backout		Avg.	
	Ft (N)	Fc (N)	Ft (N)	Fc (N)	Ft (N)	Fc (N)
2.5	6.2	6.1	5	5.4	5.6	5.75
1.5	3.2	3.3	2.4	2.9	2.8	3.1
0.5	1.62	1.36	1.4	1.3	1.51	1.33
0.1	2.2	0.6	2.1	0.7	2.15	0.65

Table 10-2: Force data for Al6061, 2 μ m depth of cut

Plunge/Backout	Disk	Cutting Dist. (km)	Avg. Thrust Force (N)	Avg. Cut Force (N)	Avg. Thrust Force (Plunge & Backout) (N)	Avg. Cut Force (Plunge & Backout) (N)	Ft StDev	Fc StDev
P	A	0	1.25	2.71	1.25	2.71	0.147594	0.122086
P	B	2.5	2.5	3.8			0.425395	0.287315
P	C	5	1.78	3	1.955	3.15	0.163187	0.127142
B	C	7.5	2.8	3.8				
P	D	7.5	2.3	3.6	2.55	3.7	0.186002	0.125831
B	D	10	3	4.2	3	4.2	0.22931	0.152298

Table 10-3: Wear measurements for Al6061, 2 μ m depth of cut

Cutting Dist. (km)	Edge Rad (μ m)	Wear Land (μ m)	Total Worn Area (μ m ²)	Worn Volume (μ m ³)
0	0.03	0.00	0.00	0.00
2.5	0.14	1.20	0.10	80.03
5	0.17	1.96	0.24	197.96
7.5	0.30	2.99	0.59	476.14
10	0.30	4.45	1.21	979.57

Table 10-4: Determination of Archard Wear coefficient for diamond tool machining Al6061

Sliding Dist., d_s	Thrust Force, F_T	Cut Force, F_C	Calc'd Flank Force, F_f	$F_f * d_s$	Wear Volume
km	N	N	N	N-m	μ m ³
2.5	1.25	2.71	1.002	2505	80.03
5	1.96	3.15	0.872	4360	197.96
7.5	2.56	3.7	1.298	9735	476.14
10	3	4.2	1.587	15870	979.57

10.2 TOOL FORCE AND WEAR DATA FOR CHEMICAL WEAR EXPERIMENTS ON ST1215

Table 10-5: Force data for St1215, 1 μm depth of cut, 2 m/s machine speed

Cutting Distance (m)	Avg. Thrust Force (N)	Thrust Std. Dev.	Avg. Cut Force (N)	Cut St. Dev
5	4.248975	0.330505	6.30298	0.328852
10	4.340639	0.508123	6.561906	0.414594
15	4.672194	0.523126	6.828383	0.472865
20	4.606792	0.567925	6.812712	0.452991

Table 10-6: Wear measurements for St1215, 1 μm depth of cut, 2 m/s machine speed

Cutting Dist. (m)	Edge Rad (μm)	Wear Land (μm)	R/L	Worn Area from EBID (nm^2)	Worn Volume (μm^3)
0	0.02	0			0
5	0.0741944	0.6132178	0.120992	83429	100.9491
10	0.0938443	0.578495	0.162221	71381.6	86.37174
15	0.1053176	0.8627869	0.122067	171742.3	207.8082
20	0.1297076	0.8182157	0.158525	169376	204.945

Table 10-7: Force data for St1215, 1 μm depth of cut, 1 and 4 m/s machine speed

Cut Speed	1.06 m/s				4.24 m/s			
	Thrust Force (N)	StDev	Cut Force (N)	StDev	Thrust Force (N)	StDev	Cut Force (N)	StDev
16	4.1	0.6	7.0	0.6				
20					4.0	0.3	6.8	0.3
46	4.2	0.8	6.9	0.8				
60					3.6	0.3	6.0	0.4
66	4.0	0.8	7.0	0.8				
100					4.0	0.5	7.1	0.5
166	4.3	1.4	7.3	1.4				
180					4.1	0.5	7.2	0.5
200					4.0	0.5	7.0	0.5
AVERAGE	4.2	0.9	7.1	0.9	3.9	0.4	6.8	0.4

Table 10-8: SWLI Wear land to EBID Worn Area conversion calculations,

CutSpeed (m/s)	Material	Dist (m)	Mean WLI Wear Land (μm)	EBID Wear Land (μm)	Equivalent EBID Wear Land from WLI Wear Land (μm)	EBID Area (μm^2)	Equivalent WLI Area (μm^2)	Land Error	Area Error
1	ST1215	1	0.99	0.95	0.9431438	0.179	0.19606055	0.72%	9.5%
1	ST1215	4	1.03	0.95	0.9552142	0.171	0.2021274	0.55%	18.2%
1	ST1215	216	2.03	1.82	1.8164942	1.037	1.03745186	0.19%	0.0%
4	ST1215	200	1.57	1.29	1.2866662	0.46	0.42963804	0.26%	6.6%

10.3 ADVANTEDGE FE CUTTING SIMULATION DATA

Table 10-9: AdvantEdge FE cutting model verification. Tool forces for St1118 at 1 μm depth of cut, 2.12 m/s machine speed

Simulation Name	Friction Coefficient	FcAvg N	StDev N	Err	FtAvg N	StDev N	Err
Experimental Values		6.5		0.0%	4.5		0.0%
St1118_1umDoC_2m_mu02	0.2	4.09	1.55	58.9%	2.14	1.17	110.2%
St1118_1umDoC_2m_mu05	0.5	5.22	1.45	24.5%	3.28	1.21	37.0%
St1118_1umDoC_2m_mu07	0.7	5.81	1.61	11.8%	4.07	1.26	10.5%
St1118_1umDoC_2m_mu08	0.8	6.19	1.91	5.0%	4.60	2.23	2.1%

Table 10-10: AdvantEdge FE cutting model verification. Determination of friction angle for St1118 at 1 μm depth of cut, 2.12 m/s machine speed

Simulation Name	Friction Angle deg	Err	R = Fc/Ft	Std Dev of R	Std Dev of Frict Angle deg
Experimental Values	55.30	0.0%			
St1118_1umDoC_2m_mu02	62.38	11.3%	1.91	0.32	0.00
St1118_1umDoC_2m_mu05	57.84	4.4%	1.59	0.15	0.00
St1118_1umDoC_2m_mu07	54.98	0.6%	1.43	0.06	0.00
St1118_1umDoC_2m_mu08	53.40	3.6%	1.35	0.24	0.00

Table 10-11: AdvantEdge FE cutting model verification. Shear angle, max tool temp, and shear angle for St1118 at 1 μm depth of cut, 2 m/s machine speed.

Simulation Name	Simulation Chip Width μm	Simulation Shear angle deg	Max Tool Temp ($^{\circ}\text{C}$)	StDev	Simulation Chip Width (μm) μm	Simulation Shear angle deg
Experimental Values	1.2				1.2	
St1118_1umDoC_2m_mu02	2.65	20.67	39.24	0.25	2.65	20.67
St1118_1umDoC_2m_mu05	3.44	16.21	42.53	0.20	3.44	16.21
St1118_1umDoC_2m_mu07	3.72	15.05	44.14	0.21	3.72	15.05
St1118_1umDoC_2m_mu08	3.86	14.52	45.71	0.40	3.86	14.52

Table 10-12: AdvantEdge FE cutting model maximum tool temperature for St1118, 1 μm depth of cut.

Cut Speed	Cut Force	Thrust Force	Max Tool Temp	Max Chip Temp
m/s	N	N	C	C
1.06	5.2	3.2	31	45.3
2.12	5.2	3.2	41.5	66.9
4.24	5.3	3.3	61	103.9
8	5.6	3.5	98.5	166.8
12	6	3.6	136	230.1
* Tests above 12 m/s had runtime error				